

The p -Version of the Finite Element and Finite Cell Methods

Alexander Düster¹, Ernst Rank² and Barna Szabó³

¹Hamburg University of Technology, Hamburg, Germany

²Institute for Advanced Study, Technical University of Munich, Munich, Germany

³Washington University, St. Louis, MO, USA

1	Introduction	1
2	Implementation	2
3	Convergence Characteristics	9
4	Performance Characteristics	15
5	Applications of High-Order Finite Elements to Nonlinear Problems	18
6	The Finite Cell Method	20
7	Conclusions	31
	Notes	31
	References	32
	Further Reading	35

1 INTRODUCTION

The term “ p -version of the finite element method” (FEM) first appeared in a publication by Babuška *et al.* (1981) where the theoretical foundations of a discretization strategy, in which the finite element mesh is fixed and the polynomial degree p of the elements is progressively increased, were established. That investigation was motivated by research published earlier by Szabó and Mehta (1978) where it was demonstrated on the basis of a two-dimensional problem of linear elastic fracture mechanics that increasing the

polynomial degree of elements on a fixed mesh results in a rate of convergence in energy norm that is faster than if fixed p and uniform or quasi-uniform mesh refinement, known as the h -version, were used. The symbol h refers to the diameter of the largest element in a mesh.

Today, the distinction between the h - and p -versions exists primarily for historical and theoretical reasons. In the sense that any implementation of the p -version can be used in such a way that p is fixed and the mesh is progressively refined, the h -version can be viewed as a subset of the p -version. In practical applications, the design of the mesh and the choice of the polynomial degrees are both important. In fact, it is possible to realize exponential rates of convergence when the p -version is used in combination with proper mesh design. This point was discussed from the engineering perspective by Szabó (1986) and from the theoretical perspective by Guo and Babuška (1986). Adaptive mesh refinement in conjunction with the p -version was investigated by Rank and Babuška (1987). A realization of exponential rates of convergence for Maxwell equations was discussed by Costabel *et al.* (2005).

In the remainder of this section, we first recall some basic relations of the FEM. Since the finite cell method (FCM) is a high-order approach, we first consider the p -version, that is, its implementation, convergence characteristics, performance characteristics, and some applications to nonlinear problems. Afterwards we present the FCM as a high-order immersed boundary method, taking advantage of the previous formulation and discussion of the p -version.

In the following, the p -version of the FEM is presented as a method for obtaining approximate solutions to generalized

formulations of the form

$$\text{“Find } u \in X \text{ such that } \mathcal{B}(u, v) = \mathcal{F}(v) \text{ for all } v \in Y\text{”} \quad (1)$$

where u and v are scalar or vector functions in one, two, or three dimensions. In the displacement formulation of solid mechanics problems, for example, u is the displacement function, X the space of admissible displacement functions, v the virtual displacement function, Y the space of admissible virtual displacement functions, $\mathcal{B}(u, v)$ the virtual work of internal stresses, and $\mathcal{F}(v)$ is the virtual work of external forces.

More generally, u (resp. X) is called the *trial function* (resp. *trial space*) and v (resp. Y) the *test function* (resp. *test space*), $\mathcal{B}(u, v)$ is a bilinear form defined on $X \times Y$ and $\mathcal{F}(v)$ a linear functional defined on Y . Associated with the spaces X and Y are the norms $\|\cdot\|_X$ and $\|\cdot\|_Y$.

The definitive properties of bilinear forms and linear functionals are listed, for example, in Szabó and Babuška (1991), Schwab (1998), and Babuška and Strouboulis (2001).

The definitions for $\mathcal{B}(u, v)$, $\mathcal{F}(v)$, X , and Y depend on the choice of the generalized formulation and the boundary conditions. The solution domain will be denoted by Ω and the set of functions u that satisfy the condition $\mathcal{B}(u, u) \leq C < \infty$ on Ω will be called the *energy space* and denoted by $E(\Omega)$. The exact solution will be denoted by u_{EX} . The energy norm defined by

$$\|u\|_{E(\Omega)} := \sqrt{\frac{1}{2}\mathcal{B}(u, u)} \quad (2)$$

will be associated with the spaces $X \subset E(\Omega)$ and $Y \subset E(\Omega)$. It can be shown that this formulation is equivalent to the minimization of the potential energy functional defined by

$$\Pi(u) := \frac{1}{2}\mathcal{B}(u, u) - \mathcal{F}(u) \quad (3)$$

The exact solution u_{EX} of equation (1) is the minimizer of $\Pi(u)$ on the space $X \subset E(\Omega)$.

In the FEM, finite dimensional subspaces $S \subset X$ and $V \subset Y$ are constructed. These spaces are characterized by the finite element mesh, the polynomial degrees assigned to the elements, and the mapping functions. Details are given in Section 2. An approximation to u_{EX} , denoted by u_{FE} , is obtained by solving the finite dimensional problem:

$$\text{“Find } u_{\text{FE}} \in S \text{ such that } \mathcal{B}(u_{\text{FE}}, v) = \mathcal{F}(v) \text{ for all } v \in V\text{”} \quad (4)$$

The dimension of V is the number of degrees of freedom, denoted by N .

A key theorem (see **Finite Element Methods, Finite Element Methods for Elasticity with Error-Controlled Discretization and Model Adaptivity**) states that the finite element solution u_{FE} minimizes the error in energy norm

$$\|u_{\text{EX}} - u_{\text{FE}}\|_{E(\Omega)} = \min_{u \in S} \|u_{\text{EX}} - u\|_{E(\Omega)} \quad (5)$$

It is seen that the error in energy norm depends on the choice of S . Proper choice of S depends on the regularity of u_{EX} , the objectives of computation, and the desired level of precision.

Another important theorem establishes the following relationship between the error measured in energy norm and the potential energy:

$$\|u_{\text{EX}} - u_{\text{FE}}\|_{E(\Omega)}^2 = \Pi(u_{\text{FE}}) - \Pi(u_{\text{EX}}) \quad (6)$$

Proofs are available, for example, in Szabó and Babuška (1991). In the p -version, this theorem is used for a *posteriori* estimation of the error in energy norm.

The quantities of interest are functionals of u_{EX} : $\Psi_1(u_{\text{EX}})$, $\Psi_2(u_{\text{EX}}), \dots$ approximated by $\Psi_1(u_{\text{FE}})$, $\Psi_2(u_{\text{FE}}), \dots$. An important objective of finite element computations is to establish that the relative errors in the quantities of interest are small. Therefore, it is necessary to show that

$$|\Psi_i(u_{\text{EX}}) - \Psi_i(u_{\text{FE}})| \leq \tau_i |\Psi_i(u_{\text{EX}})| \quad i = 1, 2, \dots \quad (7)$$

where τ_i are prescribed tolerances.¹ Of course, $\Psi_i(u_{\text{EX}})$ is generally unknown; however, $\Psi_i(u_{\text{EX}})$ is known to be independent of the choice of the space S . Therefore, if we compute a sequence of finite element solutions corresponding to a hierarchic sequence of finite element spaces $S_1 \subset S_2 \subset S_3 \dots$, then $\Psi_i(u_{\text{FE}}) \rightarrow \Psi_i(u_{\text{EX}})$. The limiting value of $\Psi_i(u_{\text{FE}})$ and hence τ_i can be estimated.

The p -version of the FEM is well suited for the creation of hierarchic finite element spaces and hence the estimation and control of errors in terms of the quantities of interest.

2 IMPLEMENTATION

From the theoretical point of view, the quality of approximation is completely determined by the finite element space characterized by the finite element mesh Δ , the polynomial degrees of elements \mathbf{p} , and the mapping functions Q (Section 2.5). Specifically, the finite element space S is a set of functions constructed from polynomials defined on standard elements that are mapped onto the elements of the finite element mesh, subject to the appropriate continuity requirements to ensure that it is a subset of the energy space

$$S := \{u | u \in E(\Omega), u(Q^k) \in S^{p_k}, k = 1, 2, \dots, M(\Delta)\}$$

where Q^k is the mapping function for the k th element, S^{p_k} is the polynomial space of degree p_k associated with the k th element, and $M(\Delta)$ is the number of elements. Different sets

of basis functions, called *shape functions*, can be chosen to define the same finite element space; however, there are some important considerations:

1. For a wide range of mapping parameters, the round-off error accumulation with respect to increasing the polynomial degree should be as small as possible.
2. The shape functions should permit computation of the stiffness matrices and load vectors as efficiently as possible.
3. The shape functions should permit efficient enforcement of exact and minimal continuity.
4. The choice of the shape functions affects the performance of iterative solution procedures. For large problems, this can be the dominant consideration.

The first three points suggest that shape functions should be constructed from polynomial functions that have certain orthogonality properties; they should be *hierarchical*, that is, the set of shape functions of polynomial degree $p + 1$, and the number of shape functions that do not vanish at vertices, edges, and faces should be the smallest possible. Some of the shape functions used in various implementations of the p -version are described in the following.

2.1 Hierarchic shape functions for one-dimensional problems

The *classical* finite element *nodal basis functions* in one dimension on the *standard element* $\Omega_{st} = (-1, 1)$ are illustrated on Figure 1(a).

The standard shape functions are defined by the set of Lagrange polynomials

$$N_i^p(\xi) = \prod_{j=1, j \neq i}^{p+1} \frac{\xi - \xi_j}{\xi_i - \xi_j} \quad (8)$$

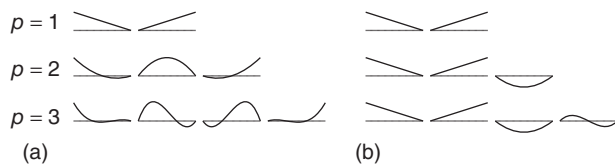


Figure 1. Set of one-dimensional standard and hierarchic shape functions for $p = 1, 2, 3$. (Reproduced with permission from Düster *et al.*, 2001. © John Wiley & Sons, 2001.)

The points ξ_j where

$$N_i^p(\xi_j) = \delta_{ij} = \begin{cases} 0 & \text{if } i \neq j \\ 1 & \text{if } i = j \end{cases} \quad (9)$$

are called *nodes*. There are certain advantages in selecting the nodes to be the Gauss–Lobatto points as done in the spectral element method, which is also addressed in this encyclopedia (see **Spectral Element and hp Methods**). This approach has been modified to suit the p -version of the FEM in Melenk *et al.* (2001). Note that the sum of all Lagrange polynomials for a given polynomial degree p equals unity:

$$\sum_{i=1}^{p+1} N_i^p(\xi) = 1 \quad (10)$$

Every function that can be represented as a linear combination of this standard basis can be represented also by the set of hierarchic basis functions (Figure 1b). A principal difference between the two bases is that in the hierarchic case all lower order shape functions are contained in the higher order basis. The set of one-dimensional hierarchic shape functions, introduced by Szabó and Babuška (1991), is given by

$$N_1(\xi) = \frac{1}{2}(1 - \xi) \quad (11)$$

$$N_2(\xi) = \frac{1}{2}(1 + \xi) \quad (12)$$

$$N_i(\xi) = \phi_{i-1}(\xi), \quad i = 3, 4, \dots, p + 1 \quad (13)$$

with

$$\phi_j(\xi) = \sqrt{\frac{2j-1}{2}} \int_{-1}^{\xi} L_{j-1}(x) dx \quad (14)$$

$$= \frac{1}{\sqrt{4j-2}} (L_j(\xi) - L_{j-2}(\xi)), \quad j = 2, 3, \dots \quad (15)$$

where $L_j(\xi)$ are the Legendre polynomials. The first two shape functions $N_1(\xi), N_2(\xi)$ are called *nodal shape functions* or *nodal modes*. Because

$$N_i(-1) = N_i(1) = 0, \quad i \geq 3 \quad (16)$$

the functions $N_i(\xi), i = 3, 4, \dots$ are called *internal shape functions*, *internal modes*, or *bubble modes*. The orthogonality property of Legendre polynomials implies

$$\int_{-1}^1 \frac{dN_i}{d\xi} \frac{dN_j}{d\xi} d\xi = \delta_{ij}, \quad i \geq 3 \quad \text{and} \quad j \geq 1$$

$$\text{or } i \geq 1 \quad \text{and} \quad j \geq 3 \quad (17)$$

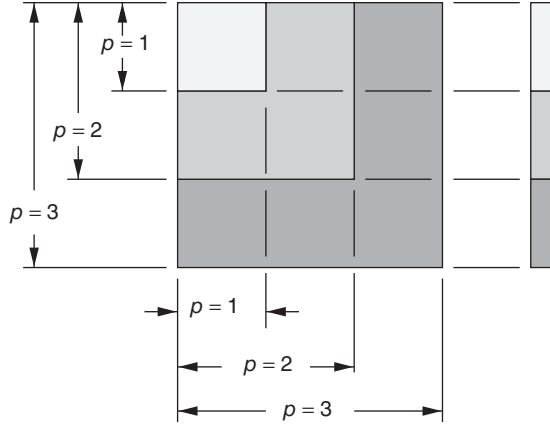


Figure 2. Hierarchic structure of stiffness matrix and load vector with $p = 3$. (Reproduced by permission of John Wiley & Sons, Ltd from E. Stein (Editor), *Error-controlled Adaptive Finite Elements in Solid Mechanics*, 263–307 (2002).)

If equations are ordered in such a way that all linear modes are numbered from 1 to n_1 , all quadratic modes are numbered from $n_1 + 1$ to n_2 , and so on, stiffness matrices corresponding to polynomial order 1 to $p - 1$ are submatrices of the stiffness matrix corresponding to polynomial order p . Figure 2 depicts the structure of a stiffness matrix and a load vector corresponding to polynomial degree of $p = 3$ schematically.

2.2 Hierarchic shape functions for quadrilaterals

The standard quadrilateral finite element is shown in Figure 3. Two types of standard polynomial spaces, the *trunk space* $S_{\text{ts}}^{p_\xi, p_\eta}(\Omega_{\text{st}}^{\text{q}})$ and the *tensor product space* $S_{\text{ps}}^{p_\xi, p_\eta}(\Omega_{\text{st}}^{\text{q}})$, are discussed in the following. The *tensor product space* $S_{\text{ps}}^{p_\xi, p_\eta}(\Omega_{\text{st}}^{\text{q}})$ consists of all polynomials on $\Omega_{\text{st}}^{\text{q}} = [(-1, 1) \times (-1, 1)]$ spanned by the set of monomials $\xi^i \eta^j$ where $i = 0, 1, \dots, p_\xi, j = 0, 1, \dots, p_\eta$, whereas the trunk space $S_{\text{ts}}^{p_\xi, p_\eta}(\Omega_{\text{st}}^{\text{q}})$ on $\Omega_{\text{st}}^{\text{q}} = [(-1, 1) \times (-1, 1)]$ is spanned by the set of all monomials

- $\xi^i \eta^j$ with $i = 0, \dots, p_\xi, j = 0, \dots, p_\eta, i + j = 0, \dots, \max\{p_\xi, p_\eta\}$
- $\xi \eta$ for $p_\xi = p_\eta = 1$
- $\xi^{p_\xi} \eta$ for $p_\xi \geq 2$
- $\xi \eta^{p_\eta}$ for $p_\eta \geq 2$.

The difference between the two standard polynomial spaces can be readily visualized when considering the spanning sets in Pascal's triangle. The set of monomials for $p_\xi = p_\eta = 3$ for both the trunk and the tensor product space is shown in Figure 4. All monomials inside the dashed line span the trunk space $S_{\text{ts}}^{3,3}(\Omega_{\text{st}}^{\text{q}})$, whereas the monomials

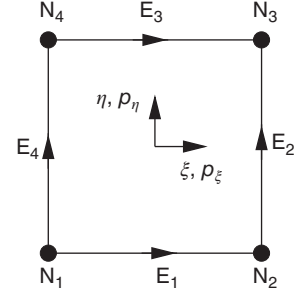


Figure 3. Standard quadrilateral element $\Omega_{\text{st}}^{\text{q}}$: definition of nodes, edges, and polynomial degrees.

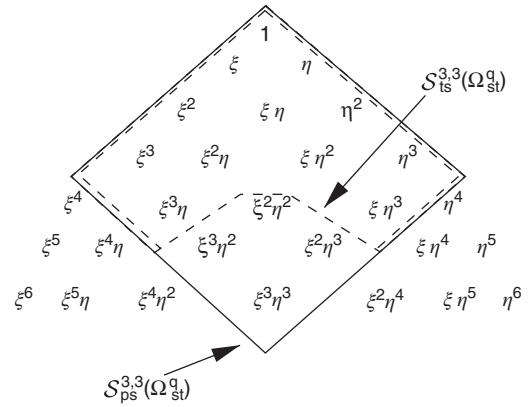


Figure 4. The trunk space $S_{\text{ts}}^{3,3}(\Omega_{\text{st}}^{\text{q}})$ and the tensor product space $S_{\text{ps}}^{3,3}(\Omega_{\text{st}}^{\text{q}})$. (Reproduced by permission of John Wiley & Sons, Ltd from E. Stein (Editor), *Error-controlled Adaptive Finite Elements in Solid Mechanics*, 263–307 (2002).)

bordered by the solid line are essential for the tensor product space $S_{\text{ps}}^{3,3}(\Omega_{\text{st}}^{\text{q}})$.

Two-dimensional shape functions can be classified into three groups: nodal, edge, and internal shape functions. Using the numbering convention shown in Figure 4, these shape functions are described in the following.

1. *Nodal or vertex modes*: The nodal modes

$$N_{1,1}^{N_i}(\xi, \eta) = \frac{1}{4}(1 + \xi_i \xi)(1 + \eta_i \eta), \quad i = 1, \dots, 4 \quad (18)$$

are the standard bilinear shape functions, well known from the isoparametric four-node quadrilateral element. (ξ_i, η_i) denote the local coordinates of the i th node.

2. *Edge or side modes*: These modes are defined separately for each edge; they vanish at all other edges. The

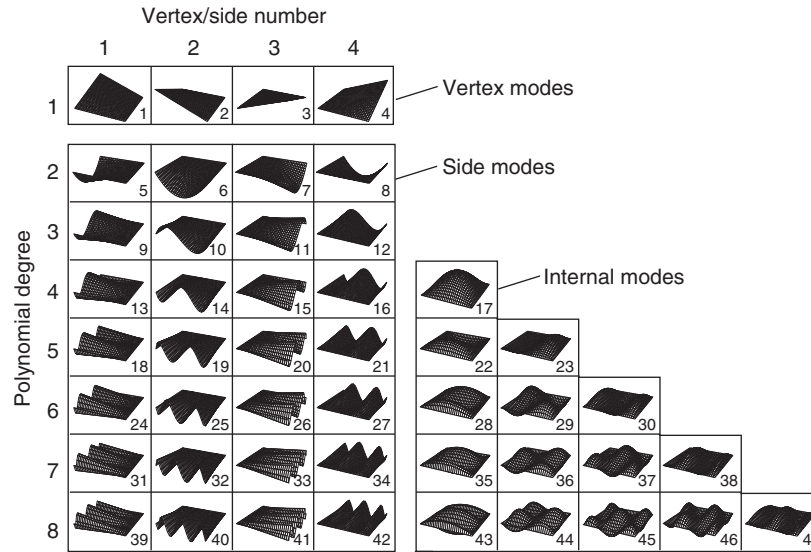


Figure 5. Hierarchic shape functions for quadrilateral elements. Trunk space, $p = 1$ to $p = 8$. (Reproduced with permission from Szabó and Babuška (1991). © John Wiley & Sons, 1991.)

corresponding modes for edge E_1 , for example, read:

$$N_{i,1}^{E_1}(\xi, \eta) = \frac{1}{2}(1 - \eta)\phi_i(\xi), \quad i \geq 2 \quad (19)$$

3. *Internal modes:* The internal modes

$$N_{i,j}^{\text{int}}(\xi, \eta) = \phi_i(\xi)\phi_j(\eta), \quad i, j \geq 2 \quad (20)$$

are purely local because they vanish at the edges of the quadrilateral element.

As already indicated, the indices i, j of the shape functions denote the polynomial degrees in the local directions ξ, η . In Figure 5, all hierarchic shape functions that span the trunk space are plotted up to order $p = 8$.

2.3 Hierarchic shape functions for hexahedrals

The implementation of high-order finite elements in three dimensions can be based on a hexahedral element formulation (Figure 6), again using the hierarchic shape functions introduced by Szabó and Babuška (1991). High-order hexahedral elements are suited for solid, “thick” structures and for thin-walled structures alike. In the case of plate- or shell-like structures, one local variable can be identified to correspond with the thickness direction and it is possible to choose the polynomial degree in the thickness direction differently from those in the in-plane direction (Düster *et al.*, 2001). Generalizing the two-dimensional concept, three-dimensional shape functions can be classified into four groups:

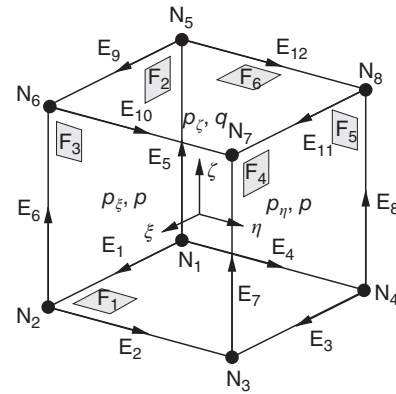


Figure 6. Standard hexahedral element Ω_{st}^h : Definition of nodes, edges, faces, and polynomial degrees.

1. *Nodal or vertex modes:* The nodal modes

$$N_{1,1,1}^{N_i}(\xi, \eta, \zeta) = \frac{1}{8}(1 + \xi_i\xi)(1 + \eta_i\eta)(1 + \zeta_i\zeta), \quad i = 1, \dots, 8 \quad (21)$$

are the standard trilinear shape functions, well known from the isoparametric eight-node brick element. (ξ_i, η_i, ζ_i) are the local coordinates of the i th node.

2. *Edge modes:* These modes are defined separately for each edge. If we consider, for example, edge E_1 (Figure 6), the corresponding edge modes read:

$$N_{i,1,1}^{E_1}(\xi, \eta, \zeta) = \frac{1}{4}(1 - \eta)(1 - \zeta)\phi_i(\xi), \quad i \geq 2 \quad (22)$$

3. *Face modes*: These modes are defined separately for each individual face. If we consider, for instance, face F_1 , the corresponding face modes read:

$$N_{i,j,1}^{F_1}(\xi, \eta, \zeta) = \frac{1}{2}(1 - \zeta)\phi_i(\xi)\phi_j(\eta), \quad i, j \geq 2 \quad (23)$$

4. *Internal modes*: The internal modes

$$N_{i,j,k}^{\text{int}}(\xi, \eta, \zeta) = \phi_i(\xi)\phi_j(\eta)\phi_k(\zeta), \quad i, j, k \geq 2 \quad (24)$$

are purely local and vanish on the faces of the hexahedral element.

The indices i, j, k of the shape functions denote the polynomial degrees in the local directions ξ, η, ζ .

Three different types of finite element spaces can be readily defined: the *trunk space* $S_{\text{ts}}^{p_\xi, p_\eta, p_\zeta}(\Omega_{\text{st}}^{\text{h}})$, the *tensor product space* $S_{\text{ps}}^{p_\xi, p_\eta, p_\zeta}(\Omega_{\text{st}}^{\text{h}})$, and an *anisotropic tensor product space* $S^{p, p, q}(\Omega_{\text{st}}^{\text{h}})$. A detailed description of these finite element spaces can be found in Szabó and Babuška (1991). The polynomial degrees for the finite element spaces $S_{\text{ts}}^{p_\xi, p_\eta, p_\zeta}(\Omega_{\text{st}}^{\text{h}})$ and $S_{\text{ps}}^{p_\xi, p_\eta, p_\zeta}(\Omega_{\text{st}}^{\text{h}})$ can be varied separately in each local direction (Figure 6). Differences between the trunk and product spaces occur in the face modes and internal modes only. For an explanation, we first consider the face modes, for example, the modes for face 1. Indices i, j denote the polynomial degrees of the face modes in ξ and η directions, respectively.

Face modes (face F_1): $N_{i,j,1}^{F_1}(\xi, \eta, \zeta) = 1/2(1 - \zeta)\phi_i(\xi)\phi_j(\eta)$

trunk space

$$i = 2, \dots, p_\xi - 2$$

$$j = 2, \dots, p_\eta - 2$$

$$i + j = 4, \dots, \max\{p_\xi, p_\eta\}$$

tensor product space

$$i = 2, \dots, p_\xi$$

$$j = 2, \dots, p_\eta$$

The definition of the set of internal modes is very similar. Indices i, j, k now denote the polynomial degrees in the three local directions ξ, η , and ζ .

Internal modes: $N_{i,j,k}^{\text{int}}(\xi, \eta, \zeta) = \phi_i(\xi)\phi_j(\eta)\phi_k(\zeta)$

trunk space

$$i = 2, \dots, p_\xi - 4$$

$$j = 2, \dots, p_\eta - 4$$

$$k = 2, \dots, p_\zeta - 4$$

$$i + j + k = 6, \dots, \max\{p_\xi, p_\eta, p_\zeta\}$$

tensor product space

$$i = 2, \dots, p_\xi$$

$$j = 2, \dots, p_\eta$$

$$k = 2, \dots, p_\zeta$$

The space $S^{p, p, q}(\Omega_{\text{st}}^{\text{h}})$ defines an anisotropic set of shape functions determined by two polynomial degrees p and q (Figure 6). All shape functions of higher order in ξ and η

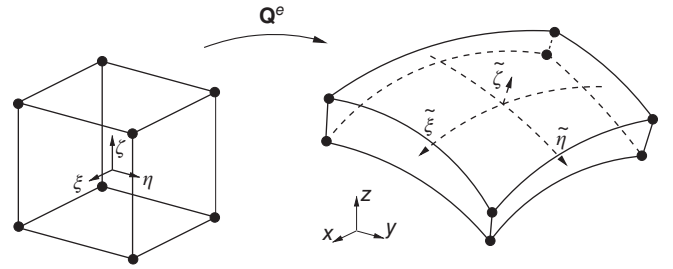


Figure 7. Modeling thin-walled structures with hexahedral elements.

directions are associated with the polynomial degree p . These shape functions correspond to the edges 1, 2, 3, 4, 9, 10, 11, 12, to the faces 1 and 6 and to all internal modes. Shape functions for faces 1 and 6 are equal to those of the trunk space $S_{\text{ts}}^{p_\xi, p_\eta, p_\zeta}(\Omega_{\text{st}}^{\text{h}})$ with $p_\xi = p_\eta = p$. The index q defines the degree of all shape functions of higher order in ζ -direction that are associated with the edges 5, 6, 7, 8, with the faces 2, 3, 4, 5, and with all internal modes. The modes corresponding to the faces 2, 3, 4, 5 are equal to those of the tensor product space $S_{\text{ps}}^{p_\xi, p_\eta, p_\zeta}(\Omega_{\text{st}}^{\text{h}})$ with $p_\xi = p_\eta = p$ and $p_\zeta = q$.

Owing to the anisotropic nature of the finite element space $S^{p, p, q}(\Omega_{\text{st}}^{\text{h}})$, it is important to ensure that the local coordinate ζ of the hexahedral element corresponds to the thickness direction, as shown in Figure 7. In this way, one can introduce anisotropic element formulations for the analysis of shell-like solids, also called “thin solids” (Szabó and Sahrman, 1978; Szabó and Babuška, 1991; Düster *et al.*, 2001).

2.4 Shape functions for hierarchic plate and shell models

An alternative method for formulating shell models, including models for laminated shells, is outlined in the following. A structural shell is characterized by a surface and the thickness d . Both are given in terms of two parameters α, β :

$$x = x(\alpha, \beta), \quad y = y(\alpha, \beta), \quad z = z(\alpha, \beta), \quad d = d(\alpha, \beta)$$

Associated with each point of the mid-surface are three basis vectors. Two of the basis vectors lie in the tangent plane at the point (α, β) :

$$\mathbf{b}^{(1)} = \frac{\partial x}{\partial \alpha} \mathbf{e}_x + \frac{\partial y}{\partial \alpha} \mathbf{e}_y + \frac{\partial z}{\partial \alpha} \mathbf{e}_z \quad (25)$$

$$\mathbf{b}^{(2)} = \frac{\partial x}{\partial \beta} \mathbf{e}_x + \frac{\partial y}{\partial \beta} \mathbf{e}_y + \frac{\partial z}{\partial \beta} \mathbf{e}_z \quad (26)$$

where $\mathbf{e}_x, \mathbf{e}_y, \mathbf{e}_z$ are the Cartesian unit vectors. Note that $\mathbf{b}^{(1)}$ and $\mathbf{b}^{(2)}$ are not necessarily orthogonal. The third basis vector $\mathbf{b}^{(3)}$ is the cross-product $\mathbf{b}^{(1)} \times \mathbf{b}^{(2)}$, being normal to the tangent plane by construction. These are called curvilinear basis vectors. The normalized curvilinear basis vectors are denoted by $\mathbf{e}_\alpha, \mathbf{e}_\beta, \mathbf{e}_n$. A vector \mathbf{u} given in terms of the curvilinear basis vectors is denoted by $\mathbf{u}_{(\alpha)}$, in Cartesian coordinates by $\mathbf{u}_{(x)}$. The transformation is

$$\mathbf{u}_{(x)} = \mathbf{R}\mathbf{u}_{(\alpha)} \quad (27)$$

where the columns of the transformation matrix \mathbf{R} are the unit vectors $\mathbf{e}_\alpha, \mathbf{e}_\beta, \mathbf{e}_n$. The displacement vector components are given in the following form:

$$\begin{aligned} u_\alpha &= \sum_{i=0}^{m_\alpha} u_{\alpha|i}(\alpha, \beta) \phi_i(\nu) \\ u_\beta &= \sum_{i=0}^{m_\beta} u_{\beta|i}(\alpha, \beta) \phi_i(\nu) \\ u_n &= \sum_{i=0}^{m_n} u_{n|i}(\alpha, \beta) \phi_i(\nu) \end{aligned} \quad (28)$$

where the functions of α, β are called field functions and $\phi_i(\nu)$ are called director functions. When the material is isotropic, $\phi_i(\nu)$ are polynomials; when the shell is laminated, $\phi_i(\nu)$ are piecewise polynomials (Szabó and Babuška, 1991; Actis *et al.*, 1999). It is good practice to define $\phi_i(\nu)$ to be mutually orthogonal functions.

Introducing the mapping for the mid-surface of the e th element:

$$\alpha = Q_\alpha^e(\xi, \eta), \quad \beta = Q_\beta^e(\xi, \eta), \quad (\xi, \eta) \in \Omega_{st}^q \quad (29)$$

the field functions can be written in terms of the hierarchic shape functions for quadrilaterals, as described in Section 2.2.

Equation (28) represents a semi-discretization of the problem of fully three-dimensional elasticity, in the sense that $\phi_i(\nu)$ are fixed, and thus the problem is reduced from a three-dimensional formulation to a two-dimensional one. A particular shell model is characterized by the set of numbers (m_α, m_β, m_n) .

For example, the hierarchic shell model (1,1,0) has the same kinematic assumptions as the Naghdi shell model:

$$\begin{aligned} u_\alpha &= u_{\alpha|0}(\alpha, \beta) + u_{\alpha|1}(\alpha, \beta)\nu \\ u_\beta &= u_{\beta|0}(\alpha, \beta) + u_{\beta|1}(\alpha, \beta)\nu \\ u_n &= u_{n|0}(\alpha, \beta) \end{aligned} \quad (30)$$

It differs from the Naghdi shell model only in the definition of the material stiffness matrix. In hierarchic shell models, the material stiffness matrix is the same as in the fully three-dimensional elasticity; whereas in the Naghdi shell model, it is modified through the introduction of plane strain assumptions (Naghdi, 1973).

For flat plates, the coordinate system is chosen such that \mathbf{R} is the identity matrix. In that case, model (1,1,0) has the same form as equation (30) and it is similar to the Reissner–Mindlin model, differing only in the material stiffness matrix (Rank *et al.*, 1998). The bending and membrane terms are not coupled for plates. Triangular elements are treated analogously.

2.5 Mapping

In low-order finite element analysis (FEA), the most frequently used mapping technique for the geometric description of the domain of computation is the application of isoparametric elements where the standard shape functions are used for the geometric description of elements. The same shape functions are used for the approximation of the unknown solution and for the shape of the elements. Using elements of order $p = 1$ or $p = 2$, the boundary of the domain is approximated by a polygonal or by a piecewise parabolic curve, respectively. As the mesh is refined, the boundary of the domain is approximated more and more accurately. When using the p -version, on the other hand, the mesh remains fixed. It is therefore important to model the geometry of the structure accurately with the fixed number of elements. This calls for a method that is able to describe complex geometries using only a few elements. Gordon and Hall (1973a,b) proposed the *blending function method* that is usually applied when describing curved boundaries of p -version finite elements; see, for example, Szabó and Babuška (1991) and Düster *et al.* (2001). After introducing blending function mapping, an example will compare polynomial interpolation versus exact blending mapping and demonstrate the necessity of a precise description of geometry.

2.5.1 The blending function method

Consider a quadrilateral element, as shown in Figure 8, where edge E_2 is assumed to be part of a curved boundary. The shape of edge E_2 is assumed to be defined by a parametric function $\mathbf{E}_2 = [E_{2x}(\eta), E_{2y}(\eta)]^T$, where η is the local coordinate of the element. The transformation of the local coordinates $\xi = [\xi, \eta]^T$ into the global coordinates $\mathbf{x} = [x, y]^T = \mathbf{Q}^e = [Q_x^e(\xi, \eta), Q_y^e(\xi, \eta)]^T$ can be formulated by the two functions

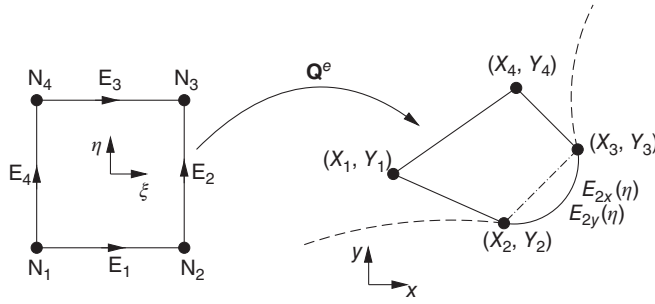


Figure 8. Blending function method for quadrilateral elements.

$$\begin{aligned}
 x &= Q_x^e(\xi, \eta) = \sum_{i=1}^4 N_{1,1}^{N_i}(\xi, \eta) X_i \\
 &\quad + \left(E_{2x}(\eta) - \left(\frac{1-\eta}{2} X_2 + \frac{1+\eta}{2} X_3 \right) \right) \frac{1+\xi}{2} \\
 y &= Q_y^e(\xi, \eta) = \sum_{i=1}^4 N_{1,1}^{N_i}(\xi, \eta) Y_i \\
 &\quad + \left(E_{2y}(\eta) - \left(\frac{1-\eta}{2} Y_2 + \frac{1+\eta}{2} Y_3 \right) \right) \frac{1+\xi}{2} \quad (31)
 \end{aligned}$$

where the first term corresponds to the standard bilinear mapping that is familiar from the isoparametric concept for quadrilateral elements with $p = 1$. The second term takes the curved edge E_2 into account. Therefore, the bilinear mapping is augmented by the blended difference between the curve $\mathbf{E}_2 = [E_{2x}(\eta), E_{2y}(\eta)]^T$ and the straight line connecting the nodes N_2 and N_3 . The blending term $(1 + \xi)/2$ ensures that the opposite edge E_4 – where $(1 + \xi)/2 = 0$ – is not affected by the curvilinear description of edge E_2 .

If a quadrilateral in which all edges are curved is to be considered, the blending function method can be expanded such that the mapping reads

$$\begin{aligned}
 x &= Q_x^e(\xi, \eta) = \frac{1}{2}(1 - \eta)E_{1x}(\xi) + \frac{1}{2}(1 + \xi)E_{2x}(\eta) \\
 &\quad + \frac{1}{2}(1 + \eta)E_{3x}(\xi) + \frac{1}{2}(1 - \xi)E_{4x}(\eta) \\
 &\quad - \sum_{i=1}^4 N_{1,1}^{N_i}(\xi, \eta) X_i \\
 y &= Q_y^e(\xi, \eta) = \frac{1}{2}(1 - \eta)E_{1y}(\xi) + \frac{1}{2}(1 + \xi)E_{2y}(\eta) \\
 &\quad + \frac{1}{2}(1 + \eta)E_{3y}(\xi) + \frac{1}{2}(1 - \xi)E_{4y}(\eta) \\
 &\quad - \sum_{i=1}^4 N_{1,1}^{N_i}(\xi, \eta) Y_i \quad (32)
 \end{aligned}$$

where

$$\begin{aligned}
 E_{ix}(\xi), E_{iy}(\xi), & \quad \text{for } i = 1, 3 \\
 E_{ix}(\eta), E_{iy}(\eta), & \quad \text{for } i = 2, 4 \quad (33)
 \end{aligned}$$

are parametric functions describing the shape of the edges $\mathbf{E}_i, i = 1, 2, 3, 4$. Therefore, the blending function method allows arbitrary parametric descriptions of the edges of elements.

2.5.2 Exact mapping versus polynomial interpolation

The following numerical example demonstrates the importance of accurate representation of geometry when a p -extension is to be applied in order to find a finite element approximation. A quarter of a linear elastic square plate with a central circular hole and unit thickness (1 mm) is loaded by a traction $t_n = 100$ MPa (Figure 9). The dimensions are chosen to be $b = h = 100$ mm and $R = 10$ mm. At the lower and right side of the plate, symmetry conditions are imposed. The isotropic linear elastic material behavior is characterized by Young's modulus $E = 206\,900$ MPa, Poisson's ratio $\nu = 0.29$, and plane stress assumptions. The strain energy of the plate – obtained by an “overkill” finite element approximation – amounts to 247.521396 Nmm. The plate is discretized by four quadrilateral elements and the circle is represented by applying

1. *exact blending*: That is, the exact parametric description of a circle is applied;
2. *parabolic description*: Two parabolas are used to interpolate the circle with a corresponding relative error $(|R - \tilde{R}|/R)100(\%) < 0.0725(\%)$, where \tilde{R} denotes the radius of the interpolated circle.

A p -extension based on the tensor product space $S_{ps}^{p,p}(\Omega_{st}^q), p = 1, \dots, 8$ is performed and the relative error in

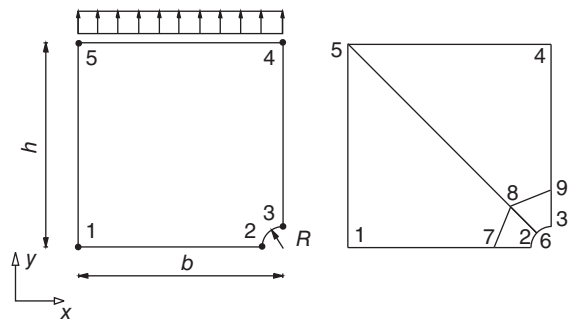


Figure 9. Perforated square plate under uniform tension.

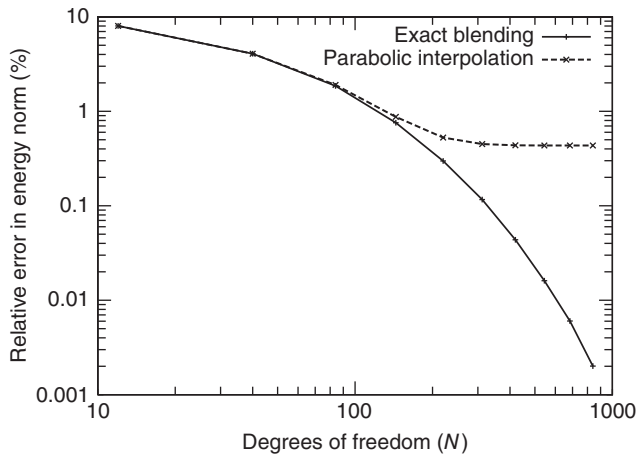


Figure 10. Influence of the blending on the relative error in energy norm.

energy norm for both the exact blending and the parabolic boundary interpolation is plotted versus the degrees of freedom on a log–log scale in Figure 10. Owing to the smoothness of the exact solution of the problem, the p -extension in conjunction with the exact blending exhibits an exponential rate of convergence (see equation (36) in Section 3.2). In the case of the piecewise parabolic boundary interpolation, the convergence rate of the p -extension deteriorates for $p \geq 3$ and the strain energy finally converges to a different value consistent with the piecewise parabolic approximation of the boundary segment. Consider the stresses, for instance, the stress component σ_{yy} in point 2; we observe that the p -extension with $p = 1, \dots, 20$ and exact blending converges rapidly while the stress obtained with parabolic boundary interpolation converges to a different value (Figure 11).

Although the relative error of the parabolic geometric interpolation appears to be small, it has a strong influence on the accuracy of the p -extension. The strain energy of the approximation converges to a different value and the stress component σ_{yy} at point 2 even diverges. The reason for this is that artificial stress singularities are introduced by the piecewise parabolic mapping. The p -extension converges to the exact solution of a different model in which the analytic arc of the circle was replaced by analytic arcs of degree 2 polynomials. Considering the first derivatives of the mapping function at the interelement node 6, and at symmetry nodes 2 and 3, discontinuities are observed. They lead to stress singularities similar to stress concentrations at corners. One way of avoiding these stress singularities is to use the exact blending or to apply quasi-regional mapping described in Királyfalvi and Szabó (1997). The idea of the quasi-regional mapping is to combine the blending function method with a polynomial

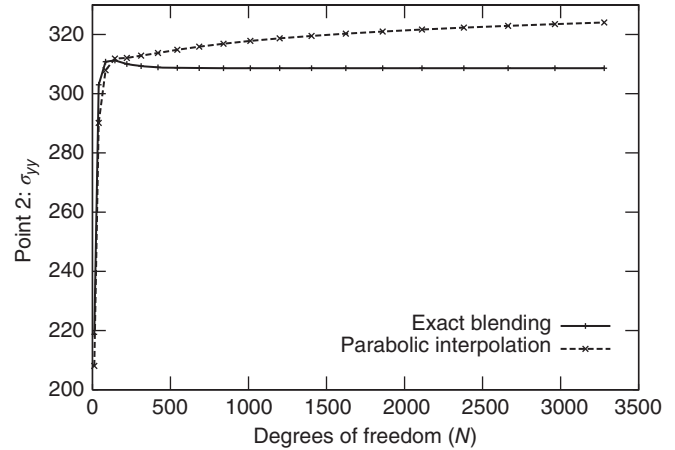


Figure 11. Influence of the blending on the stress component σ_{yy} at point 2.

interpolation of geometry, using optimal collocation points developed by Chen and Babuška (1995, 1996). A detailed comparison of exact and polynomial blending is given by Bröker (2001).

3 CONVERGENCE CHARACTERISTICS

In this section, some key theoretical results that establish relationships between the error in energy norm and the number of degrees of freedom associated with hierarchic sequences of finite element spaces: $S_1 \subset S_2 \subset \dots$ are presented.

In the early implementations of the FEM, the polynomial degrees were restricted to $p = 1$ or $p = 2$ only. Finite element spaces were enlarged by mesh refinement, that is, by reducing the diameter of the largest element, denoted by h . Subsequently, this limitation was removed, allowing enlargement of finite element spaces by increasing the polynomial degree of elements, denoted by p , while keeping the mesh fixed. To distinguish between the two approaches, the terms “ h -version” and “ p -version” gained currency. We will consider three strategies for constructing finite element spaces:

- (a) h -Extension: The polynomial degree of elements is fixed, typically at some low number, such as $p = 1$ or $p = 2$, and the number of elements is increased such that h is progressively reduced.
- (b) p -Extension: The mesh is fixed and the polynomial degree of elements is increased.
- (c) hp -Extension: The mesh is refined and the polynomial degrees of elements are concurrently increased.

A fourth strategy, not considered here, introduces basis functions, other than the mapped polynomial basis functions described in Section 2, to represent some local characteristics of the exact solution. This is variously known as the *space enrichment method*, *partition of unity method*, and *meshless method*.

It is of considerable practical interest to know how the first space S_1 should be constructed and when and how *h*-extension, *p*-extension, or *hp*-extension should be used. The underlying principles and practical considerations are summarized in the following.

3.1 Classification

It is useful to establish a simple classification for the exact solution based on *a priori* information available concerning its regularity. The exact solution, denoted by u_{EX} in the following, may be a scalar function or a vector function.

Category A: u_{EX} is analytic everywhere on the solution domain, including on the boundaries. By definition, a function is analytic in a point if it can be expanded into a Taylor series about that point. The solution is in category A also when analytical continuation is applicable.

Category B: u_{EX} is analytic everywhere on the solution domain, including on the boundaries, with the exception of a finite number of points (or in 3D, a finite number of points and edges). The locations where the exact solution is not analytic are called *singular points* or *singular edges*. The great majority of practical problems in solid mechanics belong in this category. Problems in category B are characterized by *piecewise analytic data*, that is, the domain is bounded by piecewise analytic functions and/or the boundary conditions are piecewise analytic.

Category C: u_{EX} is neither in category A nor in category B.

At corner singularities and at intersections of material interfaces in two-dimensional problems, the exact solution typically can be written in the form

$$\mathbf{u}_{\text{EX}} = \sum_{i=1}^{\infty} A_i r^{\lambda_i} \mathbf{F}_i(\theta), \quad r < \rho, \quad \lambda_{\min} > 0 \quad (34)$$

where r, θ are polar coordinates centered on the singular point, A_i, λ_i are real numbers, \mathbf{F}_i is an analytic (or piecewise analytic) vector function, and ρ is the radius of convergence. Additional details can be found in Grisvard (1985).

This is known as an asymptotic expansion of the solution in the neighborhood of a singular point. Analogous expressions can be written for one and three dimensions with $\lambda_{\min} > 1 - d/2$, where d is the number of spatial dimensions. The minimum value of λ_i corresponding to a nonzero coefficient A_i characterizes the regularity (also called “smoothness”) of the exact solution. In the following section, the key theorems concerning the asymptotic rates of convergence of the various extension processes are summarized.

3.2 A priori estimates

A priori estimates of the rates of convergence are available for solutions in categories A, B, and C. Convergence is either algebraic or exponential. The algebraic estimate is of the form

$$\|\mathbf{u}_{\text{EX}} - \mathbf{u}_{\text{FE}}\|_{E(\Omega)} \leq \frac{k}{N^\beta} \quad (35)$$

and the exponential estimate is of the form

$$\|\mathbf{u}_{\text{EX}} - \mathbf{u}_{\text{FE}}\|_{E(\Omega)} \leq \frac{k}{\exp(\gamma N^\theta)} \quad (36)$$

These estimates should be understood to mean that there exist some positive constant k , and a positive constant β (resp. γ and θ) that depend on \mathbf{u}_{EX} , such that the error will be bounded by the algebraic (resp. exponential) estimate as the number of degrees of freedom N is increased. These estimates are sharp for sufficiently large N .

The asymptotic rates of convergence for two-dimensional problems are summarized in Table 1 and for three-dimensional problems in Table 2. In these tables, p (resp. λ) represents the minimum polynomial degree assigned to the elements of a finite element mesh (resp. λ_{\min} in equation (34) (see **Finite Element Methods**)).

Remark. Note that Tables 1 and 2 indicate asymptotic rates. In some cases, entry into the asymptotic range may occur at unrealistically high p -levels, making it necessary to treat a category A problem as a category B problem. In such cases, a nearly optimal mesh layout can be constructed through proper utilization of *a priori* information. The main ideas are outlined in Szabó and Babuška (1991).

3.3 The choice of finite element spaces

The theoretical results described in Section 3.2 provide an important conceptual framework for the construction of finite element spaces (see **Interpolation and Quasi-Interpolation in *h*- and *hp*-Version Finite Element Spaces**).

Table 1. Asymptotic rates of convergence in two dimensions.

Category	Type of extension		
	h	p	hp
A	Algebraic $\beta = p/2$	Exponential $\theta \geq 1/2$	Exponential $\theta \geq 1/2$
B	Algebraic ^a $\beta = (1/2)\min(p, \lambda)$	Algebraic $\beta = \lambda$	Exponential $\theta \geq 1/3$
C	Algebraic $\beta > 0$	Algebraic $\beta > 0$	^b

^a Uniform or quasi-uniform mesh refinement is assumed. Denoting the diameter of the smallest element in the mesh by h_{\min} , a sequence of meshes is said to be quasi-uniform if h/h_{\min} is bounded. See, for example, Szabó and Babuška (2011). In the case of optimal mesh refinement, $\beta_{\max} = p/2$.

^b When \mathbf{u}_{EX} has a recognizable structure, it is possible to achieve faster than algebraic rates of convergence with hp -adaptive methods.

Table 2. Asymptotic rates of convergence in three dimensions.

Category	Type of extension		
	h	p	hp
A	Algebraic $\beta = p/3$	Exponential $\theta \geq 1/3$	Exponential $\theta \geq 1/3$
B	^a	^a	Exponential $\theta \geq 1/5$
C	Algebraic $\beta > 0$	Algebraic $\beta > 0$	^b

^a In three dimensions, \mathbf{u}_{EX} cannot be characterized by a single parameter. Nevertheless, the rate of p -convergence is at least twice the rate of h -convergence.

^b When \mathbf{u}_{EX} has a recognizable structure, it is possible to achieve faster than algebraic rates of convergence with hp -adaptive methods.

3.3.1 Problems in category A

Referring to Tables 1 and 2, it is seen that for problems in category A, exponential rates of convergence are possible through p - and hp -extensions. These convergence rates can be realized provided that all singular points lie on element vertices and edges. For both the p - and hp -extensions, the optimal mesh consists of the smallest number of elements required to partition the solution domain into triangular and quadrilateral elements in two dimensions; tetrahedral, pentahedral, and hexahedral elements in three dimensions.

When h -extensions are used, the optimal rate of convergence in 2D is algebraic with $\beta = p/2$. The optimal mesh grading depends on both p and the exact solution.

3.3.2 Problems in category B

When the exact solution can be written in the form of equation (34), there is an optimal design of the discretization in the neighborhood of the singular point. The finite

elements should be laid out so that the sizes of elements decrease in geometric progression toward the singular point (located at $x = 0$) and the polynomial degrees of elements increase away from the singular point. The optimal grading is $q = (\sqrt{2} - 1)^2 \approx 0.17$ that is independent of λ_{\min} . In practice, $q = 0.15$ is used. These are called *geometric meshes*. An example of a geometric mesh in two dimensions is given in Figure 12.

The ideal distribution of polynomial degrees is that the lowest polynomial degree is associated with the smallest element and the polynomial degrees increase linearly away from the singular points. This is because the errors in the vicinity of singular points depend primarily on the size of elements, whereas errors associated with elements farther from singular points, where the solution is smooth, depend mainly on the polynomial degree of elements. In practice, uniform p -distribution is used, which yields very nearly optimal results in the sense that convergence is exponential, and the work penalty associated with using uniform polynomial degree distribution is not substantial.

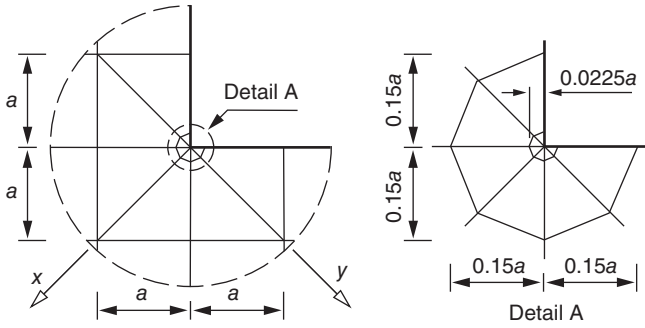


Figure 12. Example of a geometric mesh (detail).

3.4 A simple 1D model problem

In this section, we consider an axially loaded linear elastic bar, as depicted in Figure 13.

Although the solution of the underlying simple model problem (37)–(39) can be stated in a closed form, it is worth studying because it implies many of the features that also appear in more complex models. Furthermore, the general concept of the p -version can be readily represented when considering the simple one-dimensional model problem. The solution $u(x)$ (length) of the ordinary differential equation (37) describes the displacement of the bar in x -direction, being loaded by a traction $f(x)$ (force/length) and a load F (force). E (force/length²) denotes Young's modulus, A (length²) the cross-sectional area, and L (length) the length of the bar.

$$-(EAu'(x))' = f(x) \quad \text{on } \Omega = [x|0 \leq x \leq L] \quad (37)$$

$$u = 0 \quad \text{at } x = 0 \quad (38)$$

$$EAu' = F \quad \text{at } x = L \quad (39)$$

For the sake of simplicity, it is assumed that the displacement $u(x)$ and strain $\varepsilon = du/dx$ are small and that the bar exhibits a linear elastic stress–strain relationship, that is, $\sigma = E\varepsilon$ with σ being uniformly distributed over the cross-sectional area A . Equation (38) defines a Dirichlet boundary condition at $x = 0$ and equation (39), a Neumann boundary condition at $x = L$. For a detailed study of this model problem, see Szabó

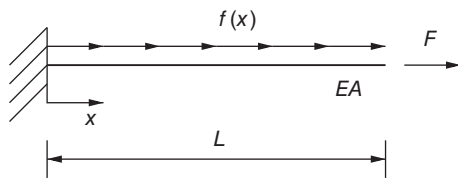


Figure 13. Linear elastic bar.

and Babuška (1991). The variational or weak formulation of the model problem (37)–(39), which is the basis for a finite element approximation can be stated as follows:

Find $u \in X$ satisfying (homogeneous) Dirichlet boundary conditions, such that

$$\mathcal{B}(u, v) = \mathcal{F}(v) \quad \text{for all } v \in Y \quad (40)$$

where

$$\mathcal{B}(u, v) = \int_0^L EAu'v' dx \quad (41)$$

$$\text{and } \mathcal{F}(v) = \int_0^L fv dx + Fv(L) \quad (42)$$

3.4.1 A numerical example with a smooth solution

Figure 13 shows an elastic bar where it is assumed that $EA = L = 1$, $f(x) = -\sin(8x)$ and $F = 0$. The p -version discretizations consist of one element with $p = 1, 2, 3, \dots, 8$, whereas the h -version is based on a uniformly refined mesh with up to eight linear ($p = 1$) elements.

First, we will consider the p -version discretization. The exact solution $u_{\text{EX}}(x) = -(1/64)\sin(8x) + (1/8)\cos(8x)$ of the problem (40)–(42) is approximated by a polynomial expression on the basis of the hierarchic shape functions (11)–(13)

$$u_{\text{FE}}(\xi) = N_1(\xi)U_1 + N_2(\xi)U_2 + \sum_{p=2}^{p_{\max}} N_{p+1}(\xi)a_{p+1} \quad (43)$$

where $p_{\max} = 8$. U_1 and U_2 denote the nodal displacements, whereas a_3, \dots, a_9 are coefficients determining the higher order terms of the approximation $u_{\text{FE}}(\xi)$. Owing to the orthonormality property (17) of the higher order shape functions, the element stiffness matrix, $K_{ij}^e = (2/L) \int_{-1}^1 EA(dN_i(\xi)/d\xi)(dN_j(\xi)/d\xi)d\xi$, $i, j = 1, 2, 3, \dots, 9$, is almost perfectly diagonal:

$$\mathbf{K}^e = \begin{bmatrix} 1 & -1 & 0 & 0 & \cdots & 0 \\ -1 & 1 & 0 & 0 & \cdots & 0 \\ 0 & 0 & 2 & 0 & \cdots & 0 \\ 0 & 0 & 0 & 2 & \cdots & 0 \\ \vdots & \vdots & \vdots & \vdots & \ddots & \vdots \\ 0 & 0 & 0 & 0 & \cdots & 2 \end{bmatrix} \quad (44)$$

Computing the element load vector, $F_i^e = (L/2) \int_{-1}^1 N_i(\xi) \times f(x(\xi))d\xi$, $i = 1, 2, 3, \dots, 9$, one finds

$$\mathbf{F}^e = [-0.1095, -0.0336, -0.0269, -0.0714, 0.0811, 0.0433, -0.0230, -0.0073, 0.0026]^T \quad (45)$$

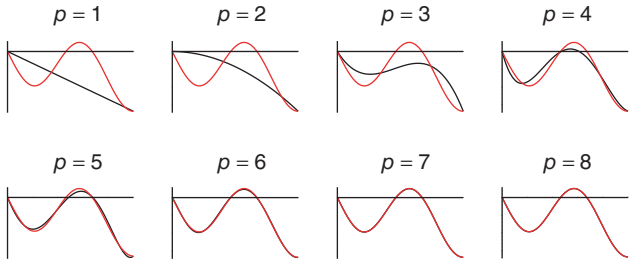


Figure 14. p -Version solution $u_{\text{FE}}(x)$ based on one element with $p = 1, 2, 3, \dots, 8$.

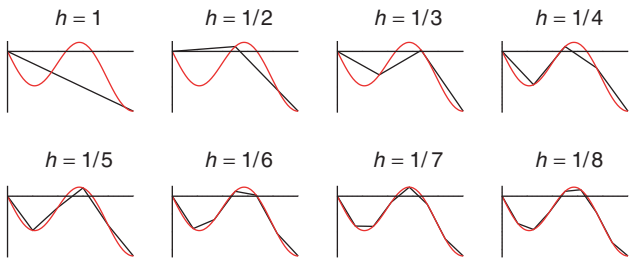


Figure 15. h -Version solution $u_{\text{FE}}(x)$ based on a uniform refined mesh with $p = 1$.

Because of the homogeneous Dirichlet boundary condition ($u(0) = u_{\text{FE}}(0) = 0 \rightarrow U_1 = 0$), the solution of the resulting diagonal equation system is trivial in this case. In Figure 14, the p -version approximation $u_{\text{FE}}(x)$ for $p = 1, 2, 3, \dots, 8$ is plotted together with the exact solution of the problem. For a first comparison of the accuracy, the same problem is solved by applying the h -version with $p = 1$ based on a uniformly refined mesh with decreasing element size $h_i = 1/i, i = 1, \dots, 8$. Again, the approximation and the exact solution are drawn (Figure 15).

In Figure 16, the relative error in energy norm

$$(e_r)_{E(\Omega)} = \frac{\|u_{\text{EX}} - u_{\text{FE}}\|_{E(\Omega)}}{\|u_{\text{EX}}\|_{E(\Omega)}} \quad (46)$$

is plotted versus the number of degrees of freedom in a double logarithmic style. By the classification given in Section 3.2, this problem is in category A, where the p -version exhibits exponential convergence (36), whereas the asymptotic rate of convergence of the h -extension is algebraic (35). For category A problems in one dimension, the parameter β in equation (35) is $\beta = p$. Since in this case $p = 1$, the asymptotic rate of convergence is 1, as shown in Figure 16.

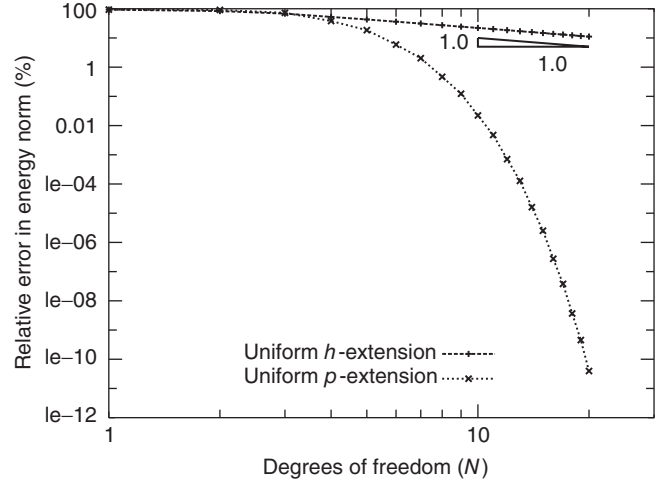


Figure 16. Comparison of the h - and p -versions: relative error in energy norm.

3.4.2 A numerical example with a nonsmooth solution

In the following example, we once again consider the weak formulation (40)–(42) of the model problem (37)–(39), where $f(x)$ is now chosen such that the exact solution is nonsmooth. We define $f(x) = \lambda(\lambda - 1)x^{\lambda-2}$, $F = 0$ and $EA = L = 1$, resulting in an exact solution $u_{\text{EX}} = -x^\lambda + \lambda x$, where λ is the parameter controlling the smoothness of the solution. If $\lambda < 1.0$, then the first derivative of the exact solution will exhibit a singularity at $x = 0$ and the given problem will be in category B. Note that $\lambda > 1/2$ is a necessary condition for obtaining a finite strain energy of the exact solution. For the following numerical example, λ is chosen to be 0.65.

In Figure 17, the relative error in energy norm (46) is plotted versus the number of degrees of freedom on a log–log scale. p -Extension was performed on one element with $p = 1, \dots, 50$, whereas the h -extension was performed on meshes with equal-sized elements $h = 1, \dots, 1/50$ with $p = 1$. Since the given problem is in category B, both extensions show algebraic convergence of type (35). The asymptotic rate of convergence of the h -extension is given by

$$\beta = \min\left(p, \lambda - \frac{1}{2}\right) = 0.15 \quad (47)$$

and can be clearly observed in Figure 17. The rate of convergence of the uniform p -extension is twice the rate of the uniform h -extension. This is due to the fact that the point where the exact solution exhibits singular behavior coincides with a node.

When combining mesh refinement with an increase in polynomial degree, exponential convergence in energy norm

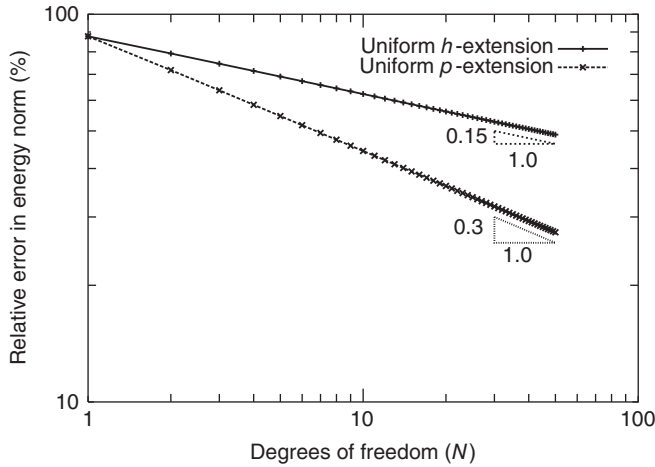


Figure 17. Comparison of the h - and p -versions: relative error in energy norm.

(36) can be achieved with an hp -extension, even when the exact solution u_{EX} has singularities. The mesh is refined toward the singular points by geometric progression using the common factor $q = 0.15$. The location of the nodal points X_i is given by

$$X_i = \begin{cases} 0 & \text{for } i = 0 \\ Lq^{n_{\text{el}}-i} & \text{for } i = 1, 2, \dots, n_{\text{el}} \end{cases} \quad (48)$$

A polynomial degree $p_{\min} = 1$ is assigned to the element at the singularity, and increases linearly away from the singular point to the maximum degree

$$p_{\max} = (2\lambda - 1)(n_{\text{el}} - 1) \quad (49)$$

where λ denotes the smoothness of the solution and n_{el} the total number of elements of the corresponding mesh. With this hp -extension, one obtains an exponential convergence in energy norm, as shown in Figure 18 (hp -version, $q = 0.15$, $\lambda = 0.65$). Using about 100 degrees of freedom, the error is by several orders of magnitude smaller than that of a uniform p -version with one element or of a uniform h -version with $p = 1$.

Figure 18 also shows the results of uniform p -extensions obtained on geometrically refined meshes with $q = 0.15$. These extensions are performed on meshes with $n_{\text{el}} = 4, 8, 12, 16, 20, 24$ elements, with p being uniformly increased from 1 to 8. In the preasymptotic range, the p -extension on fixed, geometrically graded meshes exhibits an exponential convergence rate. In the asymptotic range, the exponential convergence decreases to an algebraic rate, being limited by the smoothness λ of the exact solution. If proper meshes are used, that is, if the number of refinements

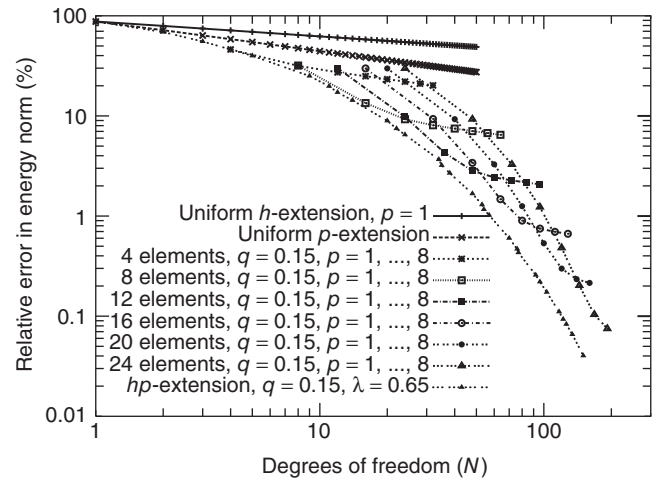


Figure 18. Comparison of the h -, p -, and hp -versions: relative error in energy norm.

corresponds to the polynomial degree, then any required accuracy is readily obtained.

3.5 Model problem: the L-shaped domain

In order to illustrate the convergence characteristics of the h -, p -, and hp -extensions for category B problems, we consider an L-shaped domain in two-dimensional elasticity, under the assumption of plane strain conditions using Poisson's ratio 0.3. In the xy -coordinate system shown in Figure 12, the exact solution (up to rigid body displacement and rotation terms) corresponding to the first term of the asymptotic expansion is

$$u_x = \frac{A_1}{2G} r^{\lambda_1} [(k - Q_1(\lambda_1 + 1)) \cos \lambda_1 \theta - \lambda_1 \cos(\lambda_1 - 2)\theta] \quad (50)$$

$$u_y = \frac{A_1}{2G} r^{\lambda_1} [(k + Q_1(\lambda_1 + 1)) \sin \lambda_1 \theta + \lambda_1 \sin(\lambda_1 - 2)\theta] \quad (51)$$

where G is the shear modulus, $\lambda_1 = 0.544483737$, $Q_1 = 0.543075579$, and $\kappa = 1.8$. The coefficient A_1 is called a *generalized stress intensity factor*. Details are available in Szabó and Babuška (1991). The corresponding stress components are

$$\sigma_x = A_1 \lambda_1 r^{\lambda_1-1} [(2 - Q_1(\lambda_1 + 1)) \cos(\lambda_1 - 1)\theta - (\lambda_1 - 1) \cos(\lambda_1 - 3)\theta] \quad (52)$$

$$\sigma_y = A_1 \lambda_1 r^{\lambda_1-1} [(2 + Q_1(\lambda_1 + 1)) \cos(\lambda_1 - 1)\theta + (\lambda_1 - 1) \cos(\lambda_1 - 3)\theta] \quad (53)$$

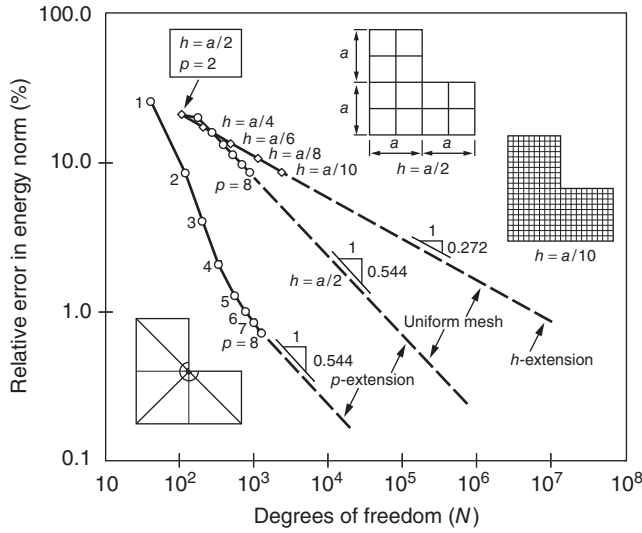


Figure 19. Convergence paths for the L-shaped domain. (Reproduced with permission from Szabó and Babuška (1991). © John Wiley & Sons, 1991.)

$$\begin{aligned} \tau_{xy} = & A_1 \lambda_1 r^{\lambda_1 - 1} [(\lambda_1 - 1) \sin(\lambda_1 - 3)\theta \\ & + Q_1(\lambda_1 + 1) \sin(\lambda_1 - 1)\theta] \end{aligned} \quad (54)$$

This model problem is representative of an important class of problems. The reentrant edges are stress-free, and the other boundaries are loaded by the tractions that correspond to the exact stress distribution given by equations (52)–(54). Since the exact solution is known, it is possible to compute the exact value of the potential energy from the definition of $\Pi(u_{\text{EX}})$ given by equation (3) and using $\mathcal{B}(u_{\text{EX}}, u_{\text{EX}}) = \mathcal{F}(u_{\text{EX}})$ from equation (1):

$$\begin{aligned} \Pi(u_{\text{EX}}) &= -\frac{1}{2} \oint [u_x(\sigma_x n_x + \tau_{xy} n_y) + u_y(\tau_{xy} n_x + \sigma_y n_y)] ds \\ &= -4.15454423 \frac{A_1 a^{2\lambda_1}}{E} \end{aligned} \quad (55)$$

where n_x, n_y are the components of the unit normal to the boundary and a is the dimension shown in Figure 12. The convergence paths for h - and p -extensions are shown in Figure 19.

It is seen that the asymptotic rates of convergence are exactly as predicted by the estimate (35). However, when p -extension is used on a geometric mesh, the preasymptotic rate is exponential or nearly so. This can be explained by observing that the geometric mesh shown in Figure 12 is overrefined for low polynomial degrees; therefore, the dominant source of the error is that part of the domain where the exact solution is smooth and hence the rate of convergence is exponential, as predicted by the estimate (36). Convergence

slows to the algebraic rate for small errors, where the dominant source of error is the immediate vicinity of the singular point.

The error estimate frequently used in conjunction with p -extensions is based on the equation (6) and the use of Richardson extrapolation utilizing the *a priori* estimate (35). When hp -adaptivity has to be considered, local-based error estimators have to be applied; see, for example, Ainsworth and Oden (2000) and Melenk and Wohlmuth (2001). By definition, the effectivity index θ is the estimated error divided by the true error. The estimated and true errors and the effectivity indices are shown in Table 3. The parameter β is the same as that in equation (35).

In order to achieve exponential rates of convergence in energy norm in the asymptotic range when the solution being approximated has singularities, sequences of finite element spaces that combine geometrically graded meshes with increasing polynomial degree must be used. In practical applications, asymptotic convergence is less important than the ability to estimate and control errors in the quantities of interest. For this reason, *a priori* information is used to design meshes in such a way that the desired levels of accuracy are realized in the quantities of interest within the range of p values allowed by the software. This discretization strategy usually results in exponential rates of convergence in the preasymptotic range. Additional discussion and examples are available in Szabó and Babuška (1991).

4 PERFORMANCE CHARACTERISTICS

We have seen in Figure 19 that for a fixed accuracy (say 1%) there is a very substantial reduction in the number of degrees of freedom when p -extension is performed on properly designed meshes. From a practical point of view, the important consideration is the cost of computational resources rather than the number of degrees of freedom. The proper basis for comparing the performance characteristics of various implementations of the h - and p -versions of the FEM is the cost of computation. The cost has to be evaluated with respect to representative model problems, such as the L-shaped domain problem discussed in Section 3.5, given specific goals of computation, the required accuracies, and the requirement that *a reasonably close estimate of the relative errors in quantities of interest* must be provided.

It is essential that comparisons of performance include a verification process, that is, a process by which it is ascertained that the relative errors in the quantities of interest are within prespecified error tolerances. Verification is understood in relation to the exact solution of the mathematical model, not in relation to some physical reality that the model

Table 3. L-shaped domain.

p	N	$\Pi(\mathbf{u}_{FE})E$	β		$(e_r)_E$ (%)		θ
		$A_1^2 a^{2\lambda_1} t_z$	Estimated	True	Estimated	True	
1	41	-3.886332	—	—	25.42	25.41	1.00
2	119	-4.124867	1.03	1.03	8.44	8.46	1.00
3	209	-4.148121	1.37	1.36	3.91	3.93	0.99
4	335	-4.152651	1.33	1.30	2.09	2.14	0.98
5	497	-4.153636	0.99	0.94	1.42	1.48	0.96
6	695	-4.153975	0.78	0.68	1.09	1.17	0.93
7	929	-4.154139	0.69	0.60	0.89	0.99	0.89
8	1199	-4.154238	0.69	0.56	0.75	0.86	0.87
∞	∞	-4.154470		0.54		0	

Geometric mesh, 18 elements, trunk space. Plane strain, $\nu = 0.3$. Estimated and true relative errors in energy norm and effectivity index θ .

is supposed to represent. The consequences of wrong engineering decisions based on erroneous information usually far outweigh the costs of verification.

Comparative performance characteristics of the h - and p -versions were first addressed in Babuška and Scapolla (1987) and Babuška and Elman (1989) through analyses of computational complexity and theoretical error estimates as well as computer timing of specific benchmark problems. The main conclusions are summarized as follows:

1. Only for the uncommon cases of very low accuracy requirements and very irregular exact solutions are low-order elements preferable to high-order elements. High-order elements typically require smaller computational effort for the same level of accuracy.
2. High-order elements are more robust than low-order elements. This point is discussed further in Section 4.1.
3. The most effective error control procedures combine proper mesh design coupled with progressive increase in p . For details, we refer to Rank and Babuška (1987), Babuška and Suri (1990), Rank (1992), and Szabó and Babuška (1991).
4. Accuracies normally required in engineering computation can be achieved with elements of degree 8 or less for most practical problems.
5. Computation of a sequence of solutions corresponding to a hierarchic sequence of finite element spaces $S_1 \subset S_2 \subset \dots$ provides for simple and effective estimation and control of error for all quantities of interest, based on various types of extrapolation and extraction procedures; see, for example, Szabó and Babuška (1988), Szabó (1990), and Yosibash and Szabó (1994).

As a general rule, for problems in categories A and B (defined in Section 3.1), which include the vast majority of practical problems in solid mechanics, p -extension on properly designed meshes is the most efficient general solution

strategy. The performance of p -extensions in solving problems on category C is discussed in Section 5.1.1.

In the p -version, the element matrices are large and their computation is time consuming. On the other hand, these operations lend themselves to parallel computation; see, for example, Rank *et al.* (2001). Furthermore, it has been shown that a substantial reduction in time can be achieved if special integration techniques are used (Nübel *et al.*, 2001), or if special shape functions and spectral quadrature techniques are used (Melenk *et al.*, 2001).

4.1 Robustness

A numerical method is said to be robust when it performs well for a broad class of admissible data. For example, in the displacement formulation of linear elasticity, letting Poisson's ratio ν approach $1/2$ causes the volumetric strain ($\text{div } \mathbf{u}$) to approach zero. This introduces constraints among the variables, effectively reducing the number of degrees of freedom, and hence causing the rate of convergence in energy norm to decrease, in some cases very substantially. This phenomenon is called *locking*. Locking also causes problems in the recovery of the first stress invariant from the finite element solution. A similar situation exists when the thickness approaches zero in plate models based on the Reissner formulation. For a precise definition of robustness, we refer to Babuška and Suri (1992). It was shown in Vogelius (1983) that the rate of convergence in p -extensions is not influenced by $\nu \rightarrow 1/2$ on straight-sided triangles. It is also known that the h -version using straight triangles does not exhibit locking, provided that $p \geq 4$. For curvilinear elements, the rate of p -convergence is slower, and for the h -version the locking problem is generally much more severe. Although the p -version is affected by membrane locking, in the range of typical plate and shell thicknesses that occur in practical engineering problems, locking effects are generally not substantial. For an investigation of membrane locking in

cylindrical shells, we refer to Pitkäranta (1992). A detailed numerical investigation of high-order finite elements for nearly incompressible hyperelastic rubber-type material has been presented in Heisserer *et al.* (2008a), showing that locking can be also overcome in the finite strain case.

4.2 Example

The following example is representative of shell intersection problems. Specifically, the intersection of two cylindrical shells is considered. Referring to Figure 20, the outside radius of shell A is $R_A = 140$ mm, and the outside radius of shell B is $R_B = 70$ mm. The wall thickness of shell A (resp. shell B) is $t_A = 8.5$ mm; (resp. $t_B = 7.5$ mm). The axes of the shells intersect at $\alpha = 65^\circ$. The length of shell A is 800 mm, and the length of shell B , measured from the point of intersection of the axes of the shells, is 300 mm. The modulus of elasticity is $E = 72.4$ MPa, and Poisson's ratio is $\nu = 0.3$.

The intersection of the outer surfaces of the shells is filleted by a “rolling ball fillet”, that is, the fillet surface is generated as if rolling a sphere of radius $r_f = 10.0$ mm along the intersection line. The mesh consists of 34 hexahedral elements. The shell intersection region, comprised of 16 elements, is the darker region shown in Figure 20. The complement is the shell region. Quasi-regional mapping utilizing 6×6 collocation points per curved face was employed.

The inside surface is loaded by a pressure \bar{p} . In order to establish equilibrium, a normal traction t_n is applied on the surface S_B , which is the surface of intersection between shell B and a plane perpendicular to its axis:

$$t_n = \frac{\bar{p}(R_B - t_B)^2}{t_B(2R_B - t_B)} \quad (56)$$

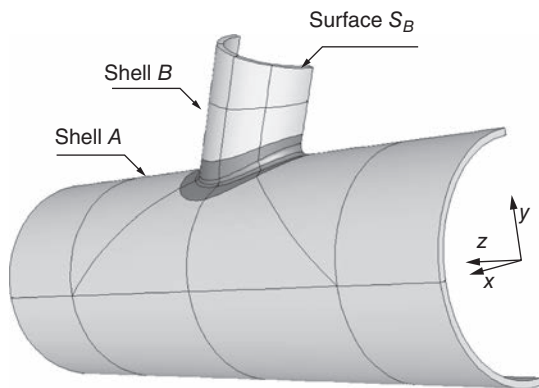
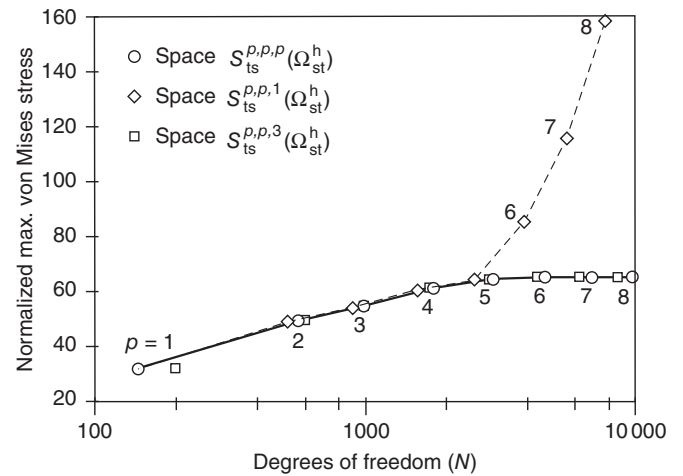


Figure 20. Example: Shell intersection problem. The darker region, comprised of 16 elements, is the shell intersection region.

The yz plane is a plane of symmetry. The other surfaces are traction-free. Appropriate rigid body constraints were imposed in order to prevent motion parallel to the plane of symmetry.

The objective is to estimate the magnitude of the maximal von Mises stress to within 5% relative error. In the shell intersection region, the solution varies substantially over distances comparable to the thickness. Therefore, dimensional reduction cannot be justified for this region. Fully three-dimensional elements, that is, elements based on the trunk spaces $S_{ts}^{p,p,p}(\Omega_{st}^h)$ with $p = 1, 2, \dots, 8$ were used in the shell intersection region, whereas the anisotropic spaces $S_{ts}^{p,p,q}(\Omega_{st}^h)$ were used in the shell region. The computations were performed with StressCheck.²

The results are shown in Figure 21. Very strong convergence to the estimated limit value of $64.7\bar{p}$ is observed when the isotropic spaces $S_{ts}^{p,p,p}(\Omega_{st}^h)$ are employed. This is true also for the anisotropic spaces $S_{ts}^{p,p,q}(\Omega_{st}^h)$ for $q \geq 2$ but not for $q = 1$. The reason is that $q = 1$ implies kinematic assumptions similar to those of the Naghdi shell theory. This introduces an artificial singularity along the faces where q changes abruptly from 8 to 1. Essentially, this is a modeling error in the sense that it pertains to the question of whether and where a particular shell model is applicable, given that the goal is to approximate some functionals of the exact solution of the underlying fully three-dimensional problem. Some aspects of this problem have been addressed in Schwab (1996), Actis *et al.* (1999), and Düster *et al.* (2007). This example illustrates the importance of convergence tests on the quantities of interest, including testing the choice of dimensionally reduced models.



5 APPLICATIONS OF HIGH-ORDER FINITE ELEMENTS TO NONLINEAR PROBLEMS

5.1 Elastoplasticity

The p - and hp -versions of the FEM have been widely accepted as efficient, accurate, and flexible methods for analyzing linear problems in computational mechanics. On the other hand, applications of the p - and hp -versions to nonlinear problems are relatively recent and hence less well known. Considering for instance, the J_2 flow theory of elastoplasticity, a loss of regularity occurs along the boundary of the plastic zone. Therefore, only an algebraic rate of convergence can be expected. However, this asymptotic rate does not give information on the preasymptotic behavior, that is, on the accuracy of a p -extension for a finite number of degrees of freedom, and especially on the question of computational investment for a desired accuracy of quantities of engineering interest.

To shed some light on this question, we investigate the deformation theory of plasticity, first proposed by Hencky (1924), as a very simple model problem for elastoplasticity. For a detailed description and numerical investigation of this model problem, see Szabó *et al.* (1995) and Düster and Rank (2001). We refer to Holzer and Yosibash (1996), Düster and Rank (2002), and Düster *et al.* (2002) for a study of the more complex and more realistic flow theory of plasticity, where each load step in an incremental analysis can be considered equivalent to the model problem investigated in the following section.

5.1.1 A benchmark problem

As a numerical example, we again use the structure of Figure 9 in Section 2.5.2 showing a quarter of a square plate with central hole and unit thickness, loaded now by a uniform tension of magnitude $t_n = 450$ MPa. The dimensions of the plate are chosen to be $b = h = 10$ mm and the radius is set to $R = 1$ mm. The material is now assumed to be elastic–perfectly plastic and plane strain conditions are assumed. The shear modulus is $\mu = 80\,193.8$ MPa, the bulk modulus is $\kappa = 164\,206.0$ MPa, and the yield stress is $\sigma_0 = 450.0$ MPa. This problem was defined by Stein (2002) as a benchmark problem for the German research project “Adaptive finite-element methods in applied mechanics”.

To find an approximate solution for the given benchmark, the p -version based on the tensor product space $S_{ps}^{p,p}(\Omega_{st}^q)$ was used, taking advantage of the blending function method to account for the exact geometry. Three different meshes with 2, 4, and 10 p -elements have been chosen (Figure 22).

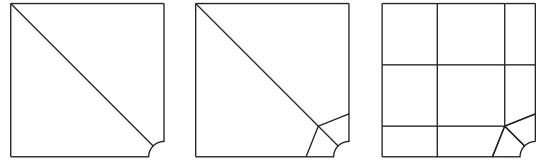


Figure 22. Three meshes with 2, 4, and 10 p -elements. (Reprinted from *Comput. Methods Appl. Mech. Engrg.*, **190**, A. Düster and E. Rank, The p -version of the finite-element method is compared to an adaptive h -version for the deformation theory of plasticity, 1925–1935, © 2001, with permission from Elsevier.)

A series of computations for polynomial degrees $p \leq 17$ for the mesh with 2 elements and $p \leq 9$ for the meshes with 4 and 10 elements was performed.

For comparisons with an adaptive h -version, we refer to the results of Barthold *et al.* (1997, 1998) and Stein *et al.* (1997) where the computations were performed with the Q1-P0 element differing from the well-known bilinear quadrilateral element by including an additional, elementwise constant pressure degree of freedom. A mesh consisting of 64 Q1-P0 elements was refined in 10 steps using the equilibrium criterion, yielding 875 elements with 1816 degrees of freedom (Figure 23). In Barthold *et al.* (1997, 1998) and Stein *et al.* (1997), the results of a sequence of graded meshes and a reference solution obtained with 24200 Q1-P0 elements with a corresponding number of 49062 degrees of freedom are also given. Comparing the results of the uniform p -version with those of the h -version based on a sequence of graded meshes, we observe that the efficiency of the p -version is superior (Figures 24 and 25). The discretization with four elements, $p = 9$, and 684 degrees of freedom provides an accuracy that is not reached by the h -version, even when using 4096 Q1-P0 elements

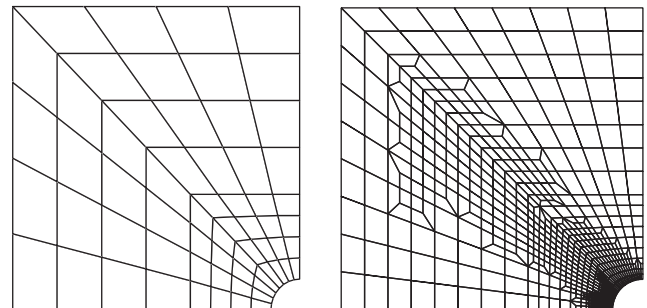


Figure 23. Initial mesh with 64 Q1-P0 elements and adapted mesh with 875 Q1-P0 elements (Barthold *et al.*, 1997). (Reprinted from *Comput. Methods Appl. Mech. Engrg.*, **190**, A. Düster and E. Rank, The p -version of the finite-element method compared to an adaptive h -version for the deformation theory of plasticity, 1925–1935, © 2001, with permission from Elsevier.)

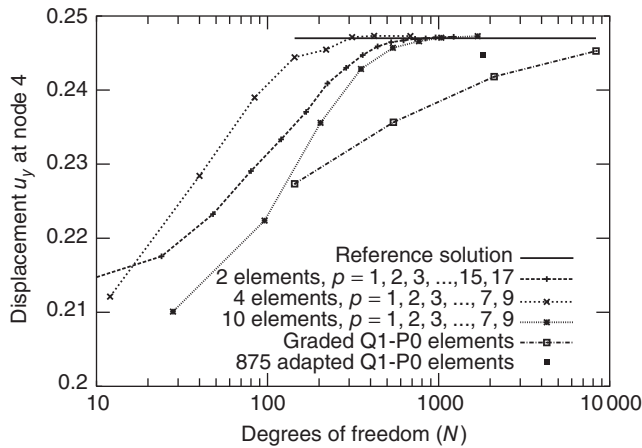


Figure 24. Displacement u_y at node 4. (Reprinted from *Comput. Methods Appl. Mech. Engrg.*, **190**, A. Düster and E. Rank, The p -version of the finite-element method compared to an adaptive h -version for the deformation theory of plasticity, 1925–1935, © 2001, with permission from Elsevier.)

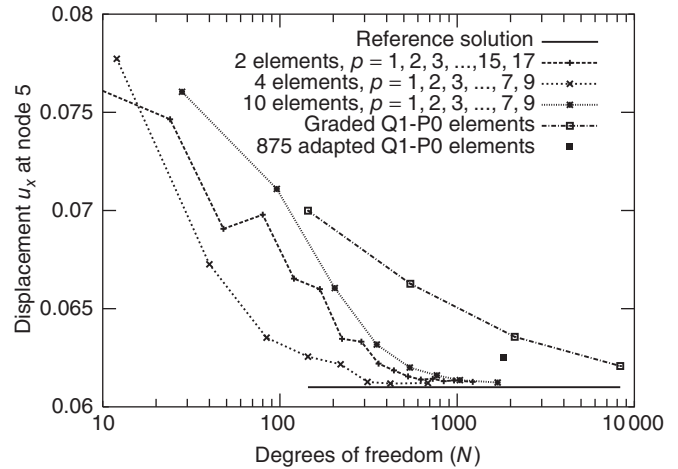


Figure 25. Displacement u_x at node 5. (Reprinted from *Comput. Methods Appl. Mech. Engrg.*, **190**, A. Düster and E. Rank, The p -version of the finite-element method compared to an adaptive h -version for the deformation theory of plasticity, 1925–1935, © 2001, with permission from Elsevier.)

with 8320 degrees of freedom. Even compared to an h -refinement, resulting in an adapted mesh with 875 Q1-P0 elements, it can be seen that a uniform p -version is much more accurate. Although the operation count per degree of freedom is significantly greater for the p -version than for the h -version, investigations of the computational cost to obtain accurate and reliable results have clearly shown a superiority of high-order elements. For further information, including three-dimensional examples of the J_2 flow theory with nonlinear isotropic hardening, we refer to Düster and Rank (2001, 2002), Düster (2001), Düster *et al.* (2002), Rank *et al.* (2002), and Stein (2002). Application of the p -FEM to problems of finite strain elastoplasticity modeling the process of powder compaction has been presented in Heißerer *et al.* (2008b).

5.1.2 An industrial application

The following example is concerned with a structural component of moderate complexity, called a *dragbrace fitting*, shown in Figure 26. This part is representative of structural components used in the aerospace sector in that relatively thin plate-like regions are reinforced by integrally machined stiffeners. The overall dimensions are length $L = 219.6$ mm and width $w = 115$ mm. The material is typically aluminum or titanium, which exhibit strain hardening. For the purposes of this example, an elastic–perfectly plastic material was chosen because it poses a more challenging problem from the numerical point of view. The material properties are those of an ASTM A-36 steel; the yield point is 248 MPa, the modulus of elasticity is $E = 200$ GPa, and Poisson’s ratio is $\nu = 0.295$.

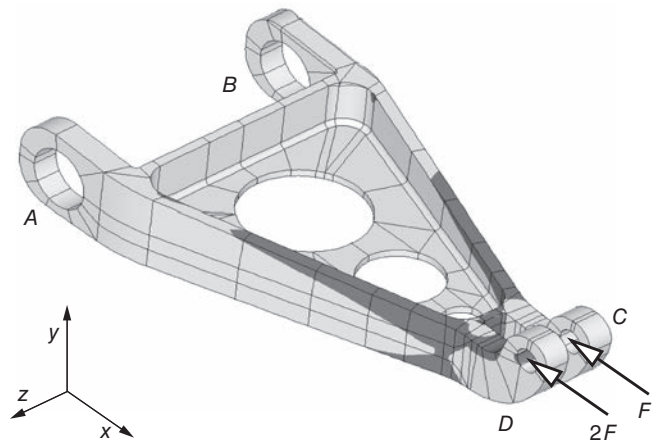


Figure 26. Example: Dragbrace fitting. Elastic–plastic solution, $p = 7$, trunk space, $N = 49\,894$. In the dark region, the equivalent strain exceeds the yield strain.

The mathematical model is based on the deformation theory of plasticity.

The lugs A and B are fully constrained and sinusoidally distributed normal tractions are applied through lugs C and D . The resultants of the tractions are F and $2F$, respectively, acting in the negative x direction as shown schematically in Figure 26. The goal of the computation is to determine the extent of the plastic zone, given that $F = 5.5$ kN. The mesh consists of 2 tetrahedral elements, 22 pentahedral elements, and 182 hexahedral elements.

The region of primary interest is the neighborhood of the loaded lugs. The results of linear analysis indicate that the maximal von Mises stress in this region is 1040 MPa, that is, 4.2 times the yield stress. Therefore, nonlinear analysis has to be performed. The region where the equivalent strain exceeds the yield strain is shown in Figure 26. The computations were performed with StressCheck.

5.2 Geometric nonlinearity

The following example illustrates an application of the p -version to a geometrically nonlinear problem. In geometrically nonlinear problems, equilibrium is satisfied in the deformed configuration. The material is assumed to be linearly elastic; however, large displacements are allowed as described in Noël and Szabó (1997). The mapping functions given by equation (32) are updated iteratively by the displacement vector components. For example, at the i th iteration, the x -coordinate of element e is mapped by

$$x^{(i)} = q_x^{(i)}(\xi, \eta, \zeta) = Q_x^e(\xi, \eta, \zeta) + u_x^{(i-1)}(\xi, \eta, \zeta) \quad (57)$$

where $u_x^{(0)} = 0$. It is known that when a thin elastic strip is subjected to pure bending, it deforms so that the curvature is constant and proportional to the bending moment:

$$\frac{1}{\rho} = \frac{M}{EI} \quad (58)$$

where ρ is the radius of curvature, M is the bending moment, E is the modulus of elasticity, and I is the moment of inertia. Poisson's ratio ν is zero. In this example, a thin strip of length $L = 100$ mm, thickness $t = 0.5$ mm, and width $b = 5$ mm is subjected to normal tractions on Face A shown in Figure 27, which correspond to M chosen so that $\rho = L/2\pi$:

$$t_n = -\frac{2\pi E}{L} \bar{y} \quad (59)$$

where \bar{y} is measured from the mid surface in the direction of the normal in the current configuration. The three displacement vector components are set to zero on Face B. Three hexahedral elements and the anisotropic space $S_{\text{is}}^{p,p,1}(\Omega_{\text{st}}^{\text{h}})$ described in Section 2.3 were used. The computations were performed with StressCheck. The load t_n was applied in 20 equal increments. The final deformed configuration, a nearly perfect cylindrical body, is shown in Figure 27. The exact solution of a perfectly cylindrical middle surface (the elastica) is the limiting case with respect to the thickness approaching zero.

This example illustrates that large aspect ratios can be used and accurate approximations achieved with the p -version even when the displacements and rotations are very large.

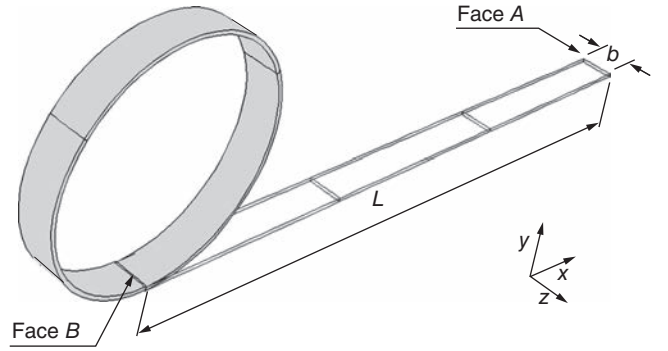


Figure 27. Example: Thin elastic strip. Geometrically nonlinear solution. Three hexahedral elements, anisotropic space $S_{\text{is}}^{8,8,1}(\Omega_{\text{st}}^{\text{h}})$, $N = 684$.

In this example, Face A was rotated 360 degrees relative to its reference position. Further applications of the p -version to hyperelastic problems including finite strains can be found in Düster *et al.* (2003). A comparison of high-order finite elements to low-order mixed element formulations for rubber-type materials undergoing large (elastic) deformations is provided in Netz *et al.* (2013).

6 THE FINITE CELL METHOD

6.1 High-order immersed boundary methods

Fictitious domain methods, also called *embedded domain methods* or *immersed boundary methods*, have been investigated by applied mathematicians for decades. The first publications date back at least to the 1960s, when Saul'ev (1963) solved boundary value problems by a fictitious domain method. Many more researchers have proposed similar approaches, for example, Neittaanmäki and Tiba (1995), Peskin (2002), Del Pino and Pironneau (2003), Mittal and Iaccarino (2005), Glowinski and Kuznetsov (2007), and Ramière *et al.* (2007). Most applications of *immersed boundary methods* can be found in computational fluid dynamics, for example, Baaijens (2001), Löhner *et al.* (2004, 2007), and Vos *et al.* (2008). In structural mechanics, only a few earlier investigations are known; see, for example, Bishop (2003). In recent years, fictitious domain methods in combination with higher order spatial approximations called the *FCM* (Parvizia *et al.*, 2007; Düster *et al.*, 2008) have attracted attention, because they offer the same high accuracy as the p -version of FEM and can be combined with other discretization strategies such as isogeometric analysis (IGA). However, they do not necessitate the generation of body-conforming finite element meshes and thus are ideal candidates for problems with highly complex geometries.

In this section, we introduce the basic idea of fictitious domain methods and present a simple numerical example demonstrating the potential of the FCM. We then address the question of how to couple the FCM to different types of geometric models and briefly discuss the numerical integration of cell matrices, when higher order shape functions are used. Next we briefly present different possibilities of how to enrich the FCM approximation locally, and finally present examples that demonstrate the power of high-order fictitious domain methods.

6.2 Basic formulation of the finite cell method

We consider a domain Ω together with an embedding domain $\Omega_e \supset \Omega$ of simpler, typically rectangular, shape together with their boundaries Γ and Γ_e , as illustrated in Figure 28 for a two-dimensional case.

We define a bilinear form

$$B_e^\alpha(\mathbf{u}, \mathbf{v}) = \int_{\Omega_e} [\mathbf{L} \mathbf{v}]^T \mathbf{C}_e^\alpha [\mathbf{L} \mathbf{u}] d\Omega \quad (60)$$

where \mathbf{u} is a displacement (trial) function, \mathbf{v} is a test function, \mathbf{L} is the standard strain-displacement operator, and $\mathbf{C}_e^\alpha = \alpha \mathbf{C}$ is the elasticity matrix of the embedding domain, with

$$\alpha(\mathbf{x}) = 1.0 \quad \forall \mathbf{x} \in \Omega \quad (61)$$

$$0.0 \leq \alpha(\mathbf{x}) < 1.0 \quad \forall \mathbf{x} \in \Omega_e \setminus \Omega \quad (62)$$

and \mathbf{C} represents the material stiffness matrix of the elasticity problem on Ω . In the case of $\alpha(\mathbf{x}) = 0$ for $\mathbf{x} \in \Omega_e \setminus \Omega$ the bilinear form (60) is

$$\begin{aligned} B_e^\alpha(\mathbf{u}, \mathbf{v}) &= \int_{\Omega_e} [\mathbf{L} \mathbf{v}]^T \alpha \mathbf{C} [\mathbf{L} \mathbf{u}] d\Omega \\ &= \int_{\Omega} [\mathbf{L} \mathbf{v}]^T \mathbf{C} [\mathbf{L} \mathbf{u}] d\Omega \\ &\quad + \int_{\Omega_e \setminus \Omega} [\mathbf{L} \mathbf{v}]^T \mathbf{0} [\mathbf{L} \mathbf{u}] d\Omega \\ &= \int_{\Omega} [\mathbf{L} \mathbf{v}]^T \mathbf{C} [\mathbf{L} \mathbf{u}] d\Omega = B(\mathbf{u}, \mathbf{v}) \end{aligned} \quad (63)$$

and the load functional

$$\begin{aligned} \mathcal{F}(\mathbf{v}) &= \int_{\Omega_e} \mathbf{v}^T (\alpha \mathbf{f}) d\Omega + \int_{\Gamma_N} \mathbf{v}^T \bar{\mathbf{t}} d\Gamma \\ &= \mathcal{F}_e^\alpha(\mathbf{v}) \end{aligned} \quad (64)$$

accounts for volume loads \mathbf{f} and prescribed tractions $\bar{\mathbf{t}}$ on the Neumann boundary of the physical domain. Note that, in general, Γ_N is *interior* to the embedding domain Ω_e . Dirichlet boundary conditions are defined likewise on Γ_D of the physical domain. The weak form of the elasticity problem on the extended domain Ω_e

$$B_e^\alpha(\mathbf{u}, \mathbf{v}) = \mathcal{F}_e^\alpha(\mathbf{v}) \quad (65)$$

is now an auxiliary problem to a classical weak form $B(\mathbf{u}, \mathbf{v}) = \mathcal{F}(\mathbf{v})$ on the physical domain Ω . The indicator function α needs to be sufficiently small in the fictitious domain, so that the error introduced by modifying the original problem is reasonably small; on the other hand, it needs to be large enough so that the condition number of the resulting system of equations will not deteriorate.

Considering now a numerical approximation to (65), we define a computational grid on the extended domain Ω_e , as shown in Figure 28. In the simplest case, a uniform Cartesian grid is used, as was suggested, for example, by Parvizian *et al.* (2007). Note that, in general, the boundary of the physical domain is *not* resolved by the grid lines. Therefore, we denote elements of the extended domain as cells Ω_c to distinguish them from classical finite elements and need to be aware that cells which are cut by the boundary of Ω have a jump in the material properties defined by \mathbf{C}_e^α . Using low-order elements, many authors assign a uniform, averaged material property to these boundary cells. This approach has been widely used in the voxel-based FEM which has been frequently applied in biomechanics, where a finite element computation is performed on the basis of a geometric model stemming from computed tomography; see, for example, Huiskes and Chao (1983). Each voxel is one trilinear hexahedral element, and material data are directly derived from the gray value of a voxel. This approach could be applied to computational domains resulting from computer-aided design (CAD) models, associating a voxel element to the material of the domain when its center of gravity is inside the domain. However, this first-order geometric resolution of the domain results in very low accuracy and nonmonotonic convergence in case of a grid refinement. For that reason, this method has not gained practical relevance, despite the advantage of a very simple coupling to the CAD model without the need to perform mesh generation.

The numerical performance of fictitious domain methods becomes very favorable when high-order approximation spaces are used. Integrated Legendre polynomials have been investigated, leading to a p -version of the FCM. As was shown in Parvizian *et al.* (2007) and Düster *et al.* (2008), exponential rates of convergence are realized with FCM

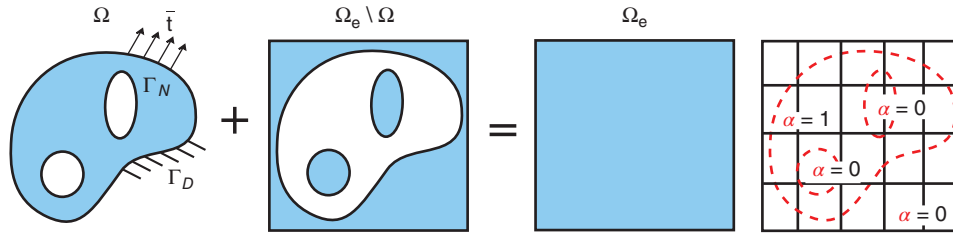


Figure 28. The physical domain Ω is embedded in Ω_e , which is meshed into a Cartesian grid. The indicator function α is introduced to define the geometry.

when smooth solutions are approximated. An efficient alternative is the B-spline version of FCM (Schillinger *et al.*, 2012c; Ruess *et al.*, 2013), where the knot-spans are used for the computational grid and shape functions of higher order and higher continuity are employed. In all cases, the discretized bilinear form reads

$$B_e^\alpha(\mathbf{u}, \mathbf{v}) = \sum_{c=1}^{n_c} \int_{\Omega_c} [\mathbf{L} \mathbf{v}]^T \alpha \mathbf{C} [\mathbf{L} \mathbf{u}] \, d\Omega \quad (66)$$

In each cell, the displacement field is approximated as

$$\mathbf{u} = \mathbf{N} \mathbf{U} \quad (67)$$

where \mathbf{N} is the matrix of shape functions and \mathbf{U} is the vector of unknowns. As usual, the product $\mathbf{L} \mathbf{N}$ is denoted as strain-displacement matrix \mathbf{B} . Based on the Bubnov–Galerkin approach, $\mathbf{v} = \mathbf{N} \mathbf{V}$, inserting (67) into (66) yields

$$\mathbf{K} \mathbf{U} = \mathbf{F} \quad (68)$$

where \mathbf{K} , the global stiffness matrix, and \mathbf{F} the global load vector are obtained by assembling all cell matrices.

The meshing process is greatly simplified by FCM; however, since the grids are not body-conforming, some algorithmic problems have to be addressed:

1. *Definition of boundary conditions.* Since the meshes are not conforming to the geometry, applications of Neumann and Dirichlet boundary conditions need special treatment. While the treatment of Neumann boundary conditions is quite straightforward, Dirichlet conditions require greater care. Homogeneous Neumann conditions (zero traction conditions) are equivalent to assuming material with zero stiffness in the embedding domain and can thus be implemented by setting $\alpha = 0$ or to a very small value outside of Ω . Nonhomogeneous Neumann boundary conditions are realized by including the second term in (64), that is, by integrating over the boundary Γ_N which is, in general, on the interior

of Ω_e . Note that in the discretized case, the integrand is a product of a function defined on the surface (the traction $\bar{\mathbf{t}}$) and the shape functions \mathbf{N} defined over cells, yet evaluated over the surface, see Düster *et al.* (2008). Dirichlet boundary conditions are best formulated in a weak sense, using Nitsche’s method. This approach has been applied in the context of the FCM in Schillinger *et al.* (2012c) and Ruess *et al.* (2013).

2. *Numerical integration of finite cell matrices.* Cells that are intersected by the boundary of the domain or internal interfaces need to be integrated with special methods to achieve the optimal convergence rate of the FCM. This issue is addressed in more detail in Section 6.5.
3. *Local enrichment.* Material interfaces, reentrant corners, and so on cause loss of regularity of the exact solution, requiring local refinement. Approaches for local refinement are summarized in Section 6.6.
4. *Solution of the resulting system of equations.* Some cells may cover only a small portion of Ω , resulting in a high condition number of the system of equations. Therefore, iterative solvers require special preconditioners. An alternative is to use direct solvers, which may limit the number of equations that can be solved. A comparison of different solution approaches for the FCM can be found in Heinze *et al.* (2014). This topic requires further investigation.

Prior to addressing the above-mentioned approaches, a simple numerical example is presented to demonstrate the appealing properties of high-order fictitious domain methods. Furthermore, in Zander *et al.* (2014) a MATLAB toolbox is presented, allowing for computations based on the FCM and supporting a rapid-prototyping of new algorithms in the context of high-order fictitious domain methods.

6.3 A first numerical example

We consider a perforated square plate under symmetry boundary conditions, as shown in Figure 29. The plate is loaded by uniform traction of 100 MPa acting in the positive

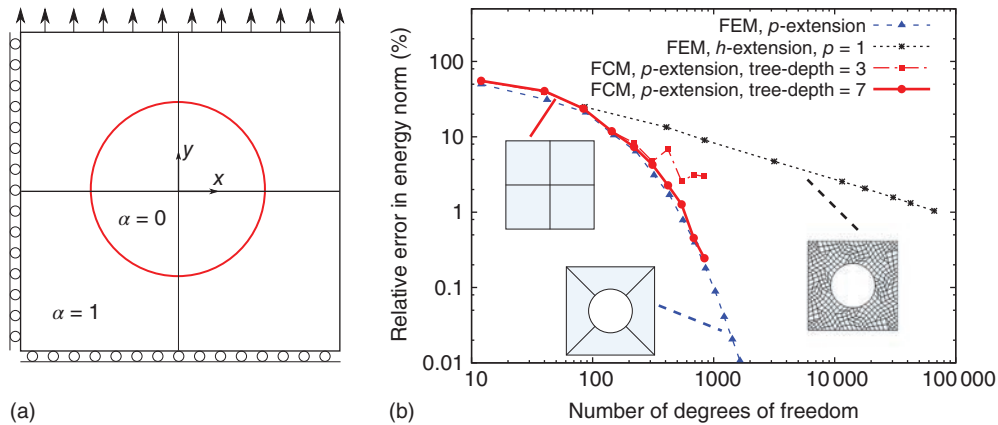


Figure 29. Perforated square plate under symmetric boundary conditions (a) and convergence of error in energy norm for different discretization methods (b).

y direction and the material is assumed to be isotropic and linear elastic. Plane stress conditions are assumed where Young's modulus is $E = 206\,900$ MPa and Poisson's ratio is $\nu = 0.29$. The dimensions of the plate are $L = B = 4$ mm and the radius of the hole is 1 mm.

Applying the FCM, the plate is meshed into 2×2 cells and the geometry of the hole is accounted for by setting $\alpha = 0$ inside the fictitious domain. The finite cells are integrated with an adaptive procedure based on a quadtree, which is explained in more detail in Section 6.5.1. To improve the quality of the FCM solution, the polynomial degree p of the hierarchic shape functions introduced in Section 2.2 is increased as $p = 1, 2, 3, \dots, 10$. The product space is used. In order to judge the efficiency of the FCM, we compare its results to a uniform h -version based on quadrilaterals of order $p = 1$ and a p -version performed on a coarse mesh consisting of four quadrilateral elements only. In the case of the p -version, we apply the blending function method described in Section 2.5.1. In this way, the circular boundary is represented exactly.

The relative error in energy norm for the different approaches is plotted in Figure 29. As expected, the h -version yields an algebraic rate of convergence, whereas the p -version converges exponentially. Although the mesh does not conform to the geometry of the hole, FCM exhibits exponential convergence, provided that the integration of the cell matrices is sufficiently accurate. Then the convergence is very similar to that of the p -version, demonstrating that the FCM is a very appealing method, which, despite the very simple discretization process, offers exponential convergence rates. It has to be noted, however, that the numerical integration of the cells plays an important role in order to obtain an optimal convergence rate. This is evident when comparing the results of the FCM for two different accuracy levels of the quadrature scheme (noted here as

tree-depth). The applied quadrature is based on a quadtree refinement (Section 6.5.1) and the tree-depth corresponds to the refinement level of the quadtree (Figure 30). Applying three refinement levels of the quadtree limits the overall accuracy of the FCM. From a certain polynomial degree on, a further p -extension does not continue to reduce the error in energy norm. This is due to the fact that the quadrature, which is closely related to the geometry error, starts to dominate the overall error. However, when choosing a more accurate integration (with tree-depth 7) the exponential convergence is continued. This demonstrates that both errors, that is, the one of the quadrature as well as of the discretization have to be properly balanced. It was proved in Dauge *et al.* (2015) that the FCM offers the possibility to achieve exponential convergence rates with a very similar performance as the p -version of the FEM.

6.4 Geometric modeling

As has been shown in Cottrell *et al.* (2009), a major part of the engineering work in industrial design and analysis cycles has to be invested in the transition from CAD-based design models to mesh-oriented FEMs. This observation with enormous practical consequence is the reason for the large success which IGA has gained over the past few years. The central idea of IGA is to apply *splines* for approximation of an unknown solution, that is, the same type of functions as for the description of the geometry of a CAD model, allowing for a smooth integration of geometric modeling and numerical computation.

IGA (see **Isogeometric Analysis: Representation of Geometry**) is especially successful for geometric models which are often used in the design of shell-like structures, where a solid can be described on the basis of curved surfaces. Considering the description of arbitrary

three-dimensional solids, geometric models can be classified into two groups: *direct* and *indirect* approaches, depending on whether the solid is described directly by its volume or by its boundary (Bungartz *et al.*, 2004). Examples for direct approaches are voxel models, octrees, or constructive solid geometry (CSG), whereas the most frequently applied indirect approach is given by boundary-representation (B-rep) models. Despite the fact that there are many different approaches to describe the geometry of a solid, one of the main advantages of the FCM is that it can be readily applied to different types of geometric models. Therefore, we briefly explain in the following sections how FCM can be combined with different geometric models, before we draw attention to the relation of the FCM and the IGA for trimmed geometric models.

6.4.1 B-rep models

B-rep models are frequently used in CAD systems to describe arbitrary three-dimensional solids. A very simple variant of B-rep models is given by the STL³ (stereolithography) format that describes unstructured triangulated surfaces bounding a solid by means of the unit normal and vertices of each of the (flat) triangles. This faceted description of boundaries is used in the FCM to incorporate nonhomogeneous Neumann or Dirichlet boundary conditions (Düster *et al.*, 2008; Ruess *et al.*, 2012). Furthermore, the faceted description can be used to decide whether a point is located within a physical domain Ω . This is of great importance when computing the cell matrices where the indicator function α accounts for the geometry during the numerical integration (see equation (66)). To this end, we apply a fast testing algorithm based on a kd-tree hierarchical radiosity method (Bindick *et al.*, 2011), which can be applied to facilitate the required information from testing against a B-rep model. It should be noted that the STL format can be readily obtained from CAD systems, such that the FCM can be directly applied to discretize B-rep models (Rank *et al.*, 2012).

6.4.2 Implicit geometry representation

Level set functions offer an elegant opportunity to describe the geometry of a body implicitly. Consider, for the sake of simplicity, the perforated square plate presented in Section 6.3. In this case, the zero iso-contour, that is, $\phi(\mathbf{x}) = 0$, of the level set function

$$\phi(\mathbf{x}) = x^2 + y^2 - R^2 \quad (69)$$

describes the circle of radius R . Utilizing the level set function, the indicator function can be defined as

$$\alpha(\mathbf{x}) = \begin{cases} 0, & \text{if } \phi(\mathbf{x}) \leq 0 \\ 1, & \text{otherwise} \end{cases} \quad (70)$$

to define the circular hole in the plate. Deriving the indicator function from a level set function enables one to describe very complex geometries without the necessity of applying B-rep models. In Joulaian and Düster (2013), high-order level set functions have been applied in the context of the FCM. It was demonstrated that a level set formulation based on Lagrange polynomials through optimized interpolation points (Chen and Babuška, 1995) allows for a very flexible and accurate discretization of curved boundaries.

6.4.3 Voxel models

Voxel models play an increasingly important role since they can be directly obtained from X-ray images and quantitative computed tomography scans (qCT-scan). This is of interest, for example, in biomechanics, material science, and many other disciplines. The geometry of the body under consideration is described by gray values of the voxels, which are used to derive local material properties of the domain of computation. In Yang *et al.* (2012a,b), it was demonstrated that a voxel model can be used to perform an efficient integration of the cell matrices and allows for fast computations of biomechanical problems, with almost no additional preprocessing effort required by segmentation of the computed tomography as is the case in standard finite element approaches. Voxel models are also a very natural starting point in order to characterize the behavior of materials with complex microstructure such as foams (Düster *et al.*, 2012; Heinze *et al.*, 2015a).

6.4.4 Constructive solid geometry presentation

CSG is a frequently applied construction paradigm used in geometric modeling of solid bodies (Bungartz *et al.*, 2004). CSG builds two- or three-dimensional bodies starting from a set of simple objects (primitives) and defines a tree of operations and transformations. The root of the tree is the final body, the leaves are the used primitives, the edges of the tree are bijective mappings transforming an object of the child node, and the nodes are Boolean set operations, that is, *union*, *intersection*, and *difference*. A combination of CSG and a finite cell approach is straightforward. We embed a CSG-domain Ω in a cube Ω_e being a superset of the CSG-body, where we define a Cartesian grid of cells. The only data to be transferred from the CSG-model to the FCM simulation is, if an integration point lies inside or outside the domain Ω , that is, an information which can efficiently be

computed by logical operations from the CSG-representation of the body (Rank *et al.*, 2012).

6.4.5 Trimmed geometric models

As mentioned at the beginning of this section, a tight connection of geometric modeling and numerical analysis is in the focus of research in the context of IGA (see **Isogeometric Analysis: Representation of Geometry**). While the power of IGA has been demonstrated in numerous fields of application, there are still many questions to be solved, among others concerning “trimmed” geometric models. Trimming is a frequently used CAD technique, where the geometry of a structure is defined as a *part* of a spline patch. Identifying the extended domain Ω_e in Figure 28 with a spline patch, such a trimming step is exactly the same concept as that applied in the FCM. The FCM, as described in this chapter, can thus immediately be interpreted as *trimming of a domain of computation* (Rank *et al.*, 2011, 2012). Most results of the FCM outlined in the context of a p -FEM discretization apply, therefore, to trimmed IGA as well. Furthermore, as shown, for example, in Schillinger *et al.* (2012a), general 3D models being geometrically described by a bi-variate, spline-based surface descriptions can be numerically analyzed by trimmed tri-variate approximation spaces. Whether these spaces should optimally be constructed in a p -FEM or a spline-based sense depends on the specific application.

6.5 Numerical integration of finite cell matrices

An accurate numerical integration of cut cells with their discontinuous integrand can be performed in various ways: There are methods that leave the integration domain unchanged, and either modify the quadrature rule (Mousavi and Sukumar, 2011; Müller *et al.*, 2013; Sudhakar and Wall, 2013) or the integrand (Ventura, 2006; Ventura and Benvenuti, 2014) to regain the accuracy of the integration. Other approaches simplify the integration by applying the divergence theorem, which reduces the dimension of the integral by one (Sudhakar *et al.*, 2014; Duzcek and Gabbert, 2015). Further approaches apply composed integration combined with a subdivision of the cut elements. Among these are adaptive quad- or octree-based integration with a refinement toward the boundary $\partial\Omega$ (Düster *et al.*, 2008). Others use an integration over a refined grid of sub-cells, allowing a pre-integration of the sub-stiffness-matrices (Yang *et al.*, 2012b). Thus, a very fast overall computation is possible (Yang *et al.*, 2012a). A few of these approaches are discussed in some more detail.

6.5.1 Adaptive integration based on spacetrees

A simple and fully automatic approach to perform an adaptive quadrature for cut cells is based on spacetrees, that is, quadtree/octree refinement in two/three dimensions, respectively. The idea is sketched in Figure 30 for the example of the perforated plate shown in Figure 29.

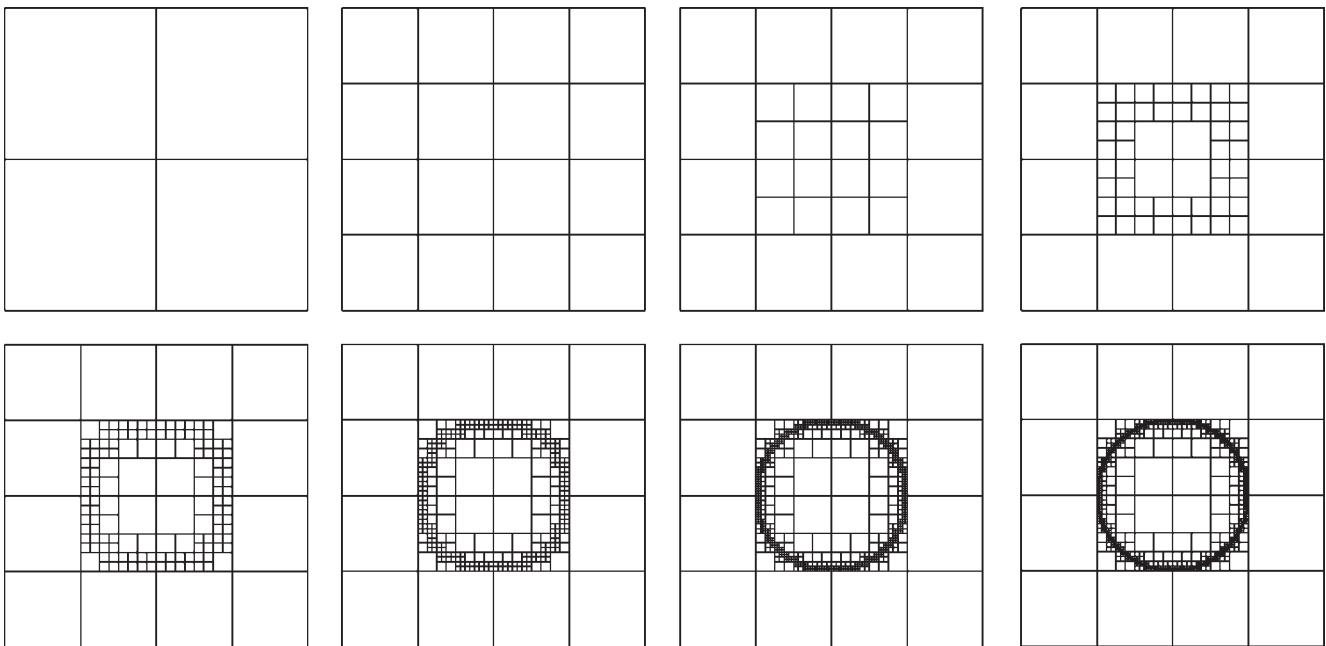


Figure 30. Perforated square plate with 2×2 cells and adaptive quadtree refinement for different tree-depth levels ranging from 1 up to 7.

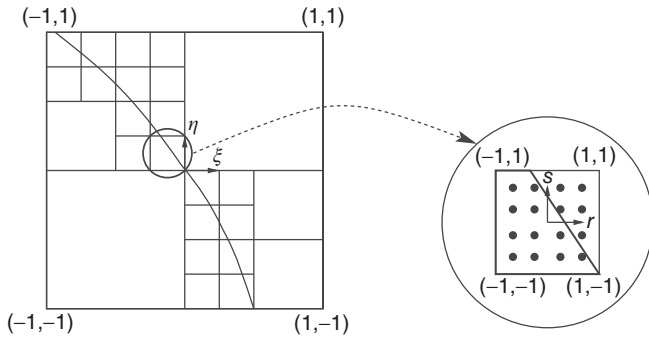


Figure 31. During the adaptive integration, the cells are subdivided into sub-cells on which a Gaussian quadrature is performed.

Cells that are broken by the boundary of the physical domain, that is, the circle, are refined into sub-cells on which the integration of the cell matrices is performed (Abadian *et al.*, 2013a). The stiffness matrix of cell c with thickness t is computed by the composed integration

$$\mathbf{K}^c = \sum_{sc=1}^{n_{sc}} \int_{s,r} \mathbf{B}^T(\xi(\mathbf{r})) \alpha(\mathbf{x}(\xi(\mathbf{r}))) \times \mathbf{CB}(\xi(\mathbf{r})) t \det \mathbf{J}^c \det \tilde{\mathbf{J}}^{c,sc} dr ds \quad (71)$$

where n_{sc} denotes the number of sub-cells within cell c , and $\xi = [\xi, \eta]^T$, $\mathbf{r} = [r, s]^T$ represent the local coordinates of the cell c and sub-cell sc , respectively. The situation is schematically sketched in Figure 31. Following the standard notation, the strain-displacement matrix is represented by \mathbf{B} . The Jacobian matrix \mathbf{J}^c is related to the mapping $\mathbf{x}(\xi)$ of the local ξ to the global $\mathbf{x} = [x, y]^T$ coordinate system. Analogously $\tilde{\mathbf{J}}^{c,sc}$ denotes the Jacobian matrix corresponding to the mapping $\xi(\mathbf{r})$, that is, from the sub-cell to the cell. Since the cells and sub-cells are usually rectangular, the mapping and, therefore, the Jacobian matrices take a simple form. To evaluate the integral (71) on each sub-cell, we apply a standard Gauss quadrature. In Abadian *et al.* (2013b), it has been demonstrated that a significant amount of numerical effort can be saved when adjusting the number of the integration points to the refinement level of the quadtree/octree. To this end, the number of integration points applied in every sub-cell is reduced according to the refinement level of the quadtree/octree.

6.5.2 A combination of spacetrees and local reparametrization

Although quadtrees and octrees offer a robust possibility to integrate the discontinuous functions inherent to finite cells cut by the boundary of a domain of computation, their major

drawback is the significant computational effort. A larger number of recursive refinements may be necessary whenever high approximation accuracy is required and, therefore, a very small integration error is mandatory. This is particularly challenging for 3D computations. Therefore, considerable effort has been invested to improve the efficiency of quadtree- and octree-based integration. In Cheng and Fries (2009) and Fries and Omerović (2015), a local mapping is used to obtain higher order approximation of the boundary. Kudela *et al.* (2015, 2016) extend this method such that topologically exceptional features of a B-rep model, such as sharp edges and corners inside a finite cell, can be handled efficiently.

This “smart octree” technique breaks down the complexity of integration of a discontinuous function in two steps. The first tries to resolve the intersection *topology* in each cut cell by subdividing it into eight generalized octants, and maps the resulting nodes and edges onto edge sections and corners of the B-rep model. If this is topologically impossible, cut cells are recursively refined by an octree-like procedure, until the local topological structure of the B-rep model can be matched. In cases where the B-rep model contains *geometry* entities (edges or faces) which are defined by parametric mapping functions like B-Splines or NURBS (nonuniform rational B-spline), the *second step* re-parametrizes the trilinear sub-cells such that they conform to the curved B-rep entity. This can be achieved by the blending function method described in Section 2.5. In Kudela *et al.* (2016), it is shown that this “smart octree” technique can easily save one order of magnitude of integration points, and thus a very significant amount of computational time.

6.5.3 Numerical integration based on moment fitting

An alternative approach to drastically reducing the number of integration points is to compute for each cut cell an individual quadrature rule. In Hubrich *et al.* (2015), the moment fitting method has been further developed for the numerical integration of discontinuities on arbitrary domains. This approach has been extended to the FCM for three-dimensional problems of solid mechanics where discontinuous integrands have to be accurately computed for cut cells, including polynomial shape functions of high order (Joulaian *et al.*, 2016).

The approach is based on four steps to set up and solve the equation system $A_{ij} w_j = b_i$, which results in the weights w_j for predefined integration points \mathbf{x}_j . In the first step, the required number of integration points, according to the desired order of the quadrature rule, is generated and the points are placed within the physical domain covered by the cut cell at hand. In the second step, the coefficient matrix $A_{ij} = f_i(\mathbf{x}_j)$ of the resulting equation system is computed, which contains the values of the polynomial basis functions

$f_i(\mathbf{x})$ evaluated at the integration points \mathbf{x}_j . Afterwards, in the third step, the right-hand side $b_i = \int_{\Omega} f_i(\mathbf{x}) \, d\Omega$ of the equation system is computed, which corresponds to the volume integrals of the basis functions over the corresponding cell. This can be easily accomplished by converting the volume integrals into surface integrals, which are numerically evaluated by applying Gaussian quadrature on triangulated surfaces. In this way, complex geometries can be handled, independent of the topology of the broken cell. Finally, in the fourth step, the resulting equation system is solved, yielding the desired weights w_j for the predefined integration points.

In Joulaian *et al.* (2016), it has been demonstrated that the proposed quadrature method can be efficiently applied to compute cell matrices independent of the geometry and topology of the cut cell. As compared to the octree approach, the number of integration points can be reduced by up to several orders of magnitude. The additional overhead introduced by the moment fitting method can be amortized in nonlinear computations, where the stiffness matrix has to be recomputed several times within the standard incremental/iterative procedure based on the Newton method.

6.6 Local enrichment

Like the p -FEM the convergence of its extension to fictitious domains, that is, the FCM is governed by the characteristics of the exact solution to be approximated (Section 3). Problems in category A converge exponentially (Dauge *et al.*, 2015), whereas problems in categories B and C converge algebraically with p -extension. If the exponential convergence property of the geometry conforming p -FEM for problems with corner or edge singularities (category B) should be recovered, an enhancement of the FCM with respect to local refinement needs to be provided. Furthermore, even for problems in category A, the grid design of finite cells should not be completely independent of the problem to be solved. As a rule of thumb, the grid size should be of the same order as local geometric features like holes or fillets of a structure. If these features are much smaller than the grid size, the expected *asymptotic* exponential convergence rate might be achieved only at high polynomial orders.

While a conformal local refinement for p -FEM toward singular points in 2D can readily be achieved by recursively applied refinement templates (see Section 3.5 with the hp -extension for the L-shaped domain), suitable conformal templates toward edge and corner singularities in 3D are already quite complex and may easily lead to an over-refinement distant from the singular zones. Like in the case of h -FEM, instead of conformal mesh refinement, nonconformal meshes and *hanging nodes* can be used (Demkowicz, 2006; Demkowicz *et al.*, 2007). An alternative

is the application of mesh overlays, which define individual finite element subspaces on a hierarchy of recursively refined meshes.

This concept was first applied by Schillinger and Rank (2011) for the FCM. A sequence of tree-like refinement patches is used to define local linear shape functions, which are added hierarchically to the p -FEM modes on the basic finite cell grid. A conforming (i.e., for second-order PDEs C^0 -continuous) approximation space is obtained by deactivating nodal modes at the boundaries of the overlay meshes. In Zander *et al.* (2015), this concept was further extended to hierarchical overlays defining not only linear but also higher order modes. With this multilevel hp -method, the FCM can exhibit the exponential rate of convergence even in the presence of singularities. Furthermore, this hierarchical concept easily allows not only a local refinement but also coarsening, which is essential in the treatment of transient problems.

When considering problems where the discontinuity or singularity in the exact solution has a known structure, one can take advantage of this knowledge and enrich the approximation space with carefully tailored Ansatz functions. In the case of sharp material interfaces, for example, an enrichment strategy based on the partition of unity method (PUM) (Melenk and Babuška, 1996) yields very efficient discretizations without the need for mesh refinement. A local enrichment strategy for the FCM, combining ideas from the hp - d -method (Rank, 1992) and the PUM has been proposed in Joulaian and Düster (2013). It has been demonstrated for two-dimensional problems of linear elasticity that the FCM can be efficiently enriched in this way, even when the geometric features of internal interfaces are very complicated.

6.7 Applications of the finite cell method

In this section, we present a brief overview of some important applications of the FCM and two examples.

So far, the FCM has been applied to a large number of problems in computational mechanics. Linear elasticity in 2D and 3D was first addressed in Parvizian *et al.* (2007) and Düster *et al.* (2008). In Rank *et al.* (2011), the FCM has been extended to the computation of curved thin-walled structures, where geometrical details of curved hexahedral cells have been taken into account in the numerical integration of the stiffness matrix. Topology optimization – which was the starting point for the development of the FCM – has been addressed in Parvizian *et al.* (2012), where it was demonstrated that the FCM supports a simple and robust procedure for finding improved structures within a fully stressed design approach. Owing to the simple meshing procedure, the FCM has been successfully applied to problems of biomechanics,

where the geometric description of the domain is given in terms of CT scans. In Ruess *et al.* (2012) and Yang *et al.* (2012a,b), the FCM has been applied to the computation of the mechanical behavior of bones.

The FCM has been also extended to the nonlinear regime. In Schillinger *et al.* (2012b,c), it was demonstrated that the FCM performs in the same way as the p -method in the case of geometrically nonlinear problems. Similar observations have been made for elastoplasticity (Abadian *et al.*, 2013b,2014); as well as for damage mechanics (Ranjbar *et al.*, 2014).

Coupled problems arising, for example, in thermoelasticity have been solved with the FCM in Zander *et al.* (2012). Furthermore, the FCM has been extended to problems of structural dynamics. In Duczek *et al.* (2014) and Joulaian *et al.* (2014), explicit time stepping schemes were combined with the FCM to simulate wave propagation through elastic materials. It has been demonstrated that the concept of spectral elements combined with the FCM, called the spectral cell method (SCM), leads to a very efficient discretization scheme. In this way, the attractive properties of high-order methods can be combined with a simple discretization scheme for wave propagation.

6.7.1 Numerical homogenization of hybrid metal foams

Owing to their low density, metal foams are attractive light-weight materials that are often applied in sandwich plates or integral foams. Additional appealing features of metal foams are their ability to absorb kinetic energy as well as their damping, insulation, and acoustic absorption properties. Open cell aluminum foam is one attractive representative of such microstructured materials. Further

improvement of the mechanical properties of aluminum foam, such as the increase of its strength, can be achieved when applying a thin coating of nanocrystalline nickel via electrodeposition.

In order to characterize such hybrid metal foams, their properties can be determined by numerical homogenization applying the FCM (Düster *et al.*, 2012). To this end, we start from a μ CT-scan of the microstructure of the metal foam. On the left-hand side of Figure 32, the corresponding voxel model of a 30 pores per inch (ppi) aluminum foam is illustrated. The size of the specimen cube is 9.6 mm. It is uniformly composed of voxels with a size of 24 μ m. In order to study the influence of the coating, we simply add a layer of additional voxels representing the nickel. The layer thickness can be defined in terms of multiple of a voxel size. On the right-hand side of Figure 32, the voxel model of the aluminum foam coated with a nickel layer of thickness 6 voxels (144 μ m) is illustrated.

The voxel model of the hybrid metal foam can be easily generated and taken advantage of in the FCM (Section 6.4.3). In Figure 33, the discretization of the coated foam with 370 398 cells of degree $p = 2$ resulting in 5 121 825 degrees of freedom is shown. In addition, the octree refinement applied for the numerical integration, as described in Section 6.5.1, is presented. The material interface is automatically detected by the adaptive integration scheme. Applying the numerical homogenization procedure presented in Heinze *et al.* (2015a), we can study the influence of the thickness of the nickel layer. In this investigation, a linear elastic material behavior with a Young's modulus of $E_{Al} = 70$ GPa for the aluminum foam and $E_{Ni} = 200$ GPa for the nickel layer is assumed. The Poisson's ratio equals to

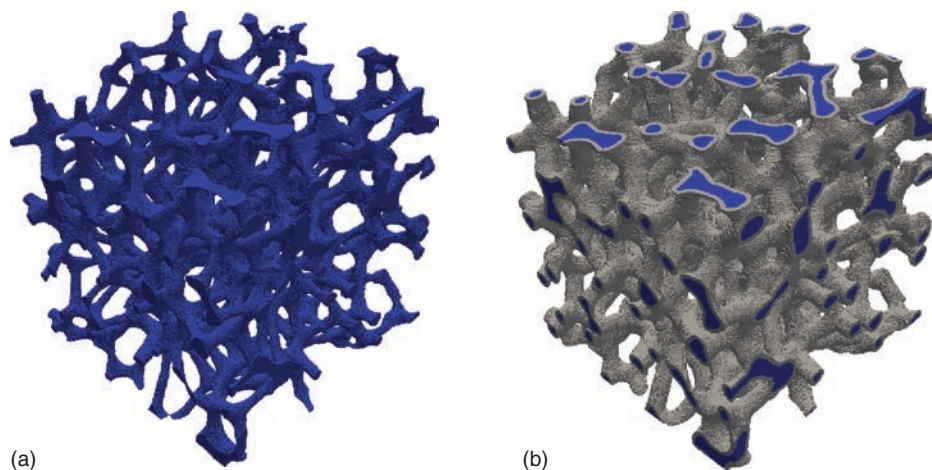


Figure 32. μ CT-scan of an aluminum foam (a) and same foam coated with a nickel layer (b). (Reprinted from Comput. Math. Appl., 70, Stephan Heinze, Meysam Joulaian, Alexander Düster, Numerical homogenization of hybrid metal foams using the finite cell method, 1501–1517, © 2015, with permission from Elsevier.)

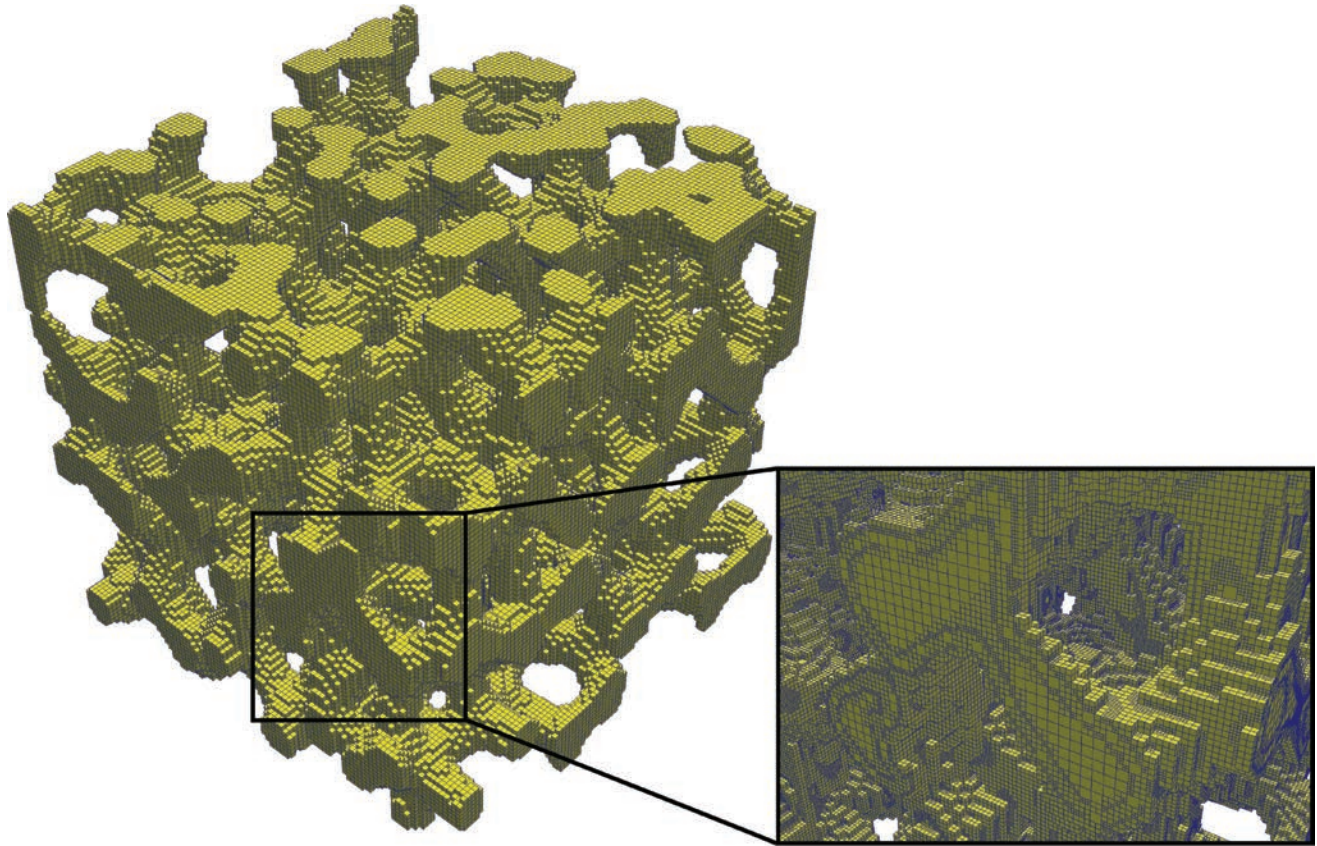


Figure 33. Finite cell mesh of the coated foam together with a detail showing the octree refinement for integration purposes. (Reprinted from *Comput. Math. Appl.*, 70, Stephan Heinze, Meysam Joulaian, Alexander Düster, Numerical homogenization of hybrid metal foams using the finite cell method, 1501–1517, © 2015, with permission from Elsevier.)

$\nu = 0.3$ for both materials. In Figure 34, the components of the effective elasticity matrix are plotted as a function of the coating thickness. As expected, the stiffness increases with the layer thickness. This approach enables us to quantify the increase of stiffness and to design hybrid metal foams with desired properties. Ongoing research is focusing on the compression of hybrid metal foams, including different sources of nonlinearities, ranging from buckling to finite strain elastoplasticity as well as self-contact.

6.7.2 Stress analysis of a human vertebra

The following example will highlight some further strengths of the FCM. A fixation of a human vertebra is analyzed, combining two different types of geometric descriptions in one analysis model. A voxel model resulting from a high-resolution medical computed tomography (HR-pQCT (high-resolution peripheral computed tomography) scan) yielding a voxel size of 0.1465 mm (Figure 35a) provides material and geometric information for the vertebra. A voxel's elasticity modulus is derived from its gray

value using a modified Keyak–Falkinstein model (Keyak and Falkinstein, 2012). A voxel with a gray value below a certain threshold is assumed to be void. The trabecular structure yielding a highly complex geometry can be seen clearly. The fixation screw (homogeneous titanium with $E = 115$ GPa, $\nu = 0.3$; see Figure 35b) is obtained as a B-rep model from a classical geometric modeler. A pullout test is simulated, where the vertebra is fixed at its top and bottom, and each screw is pulled with a force of 50 N in its axial direction.

Applying a classical FEA and resolving the vertebral structure, one has two options. In a voxel-based FEM, the screw is voxelized at the same resolution as the HR-pQCT scan, yielding a total mesh of approximately 10 million cube-shaped elements. Alternatively, a surface description of the voxel model can be generated by, for example, a marching cube algorithm. The highly complex combined surface model of screw and bone would then have to be meshed, for example, into tetrahedra. Both methods would result in an extremely high number of degrees of freedom (Wirth *et al.*, 2012).

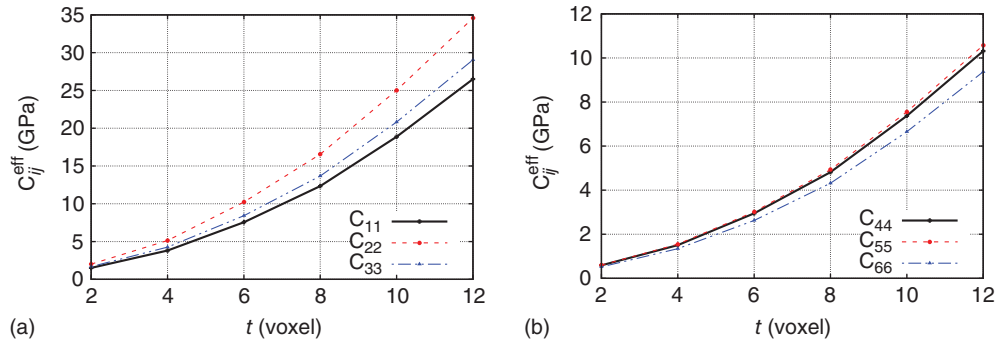


Figure 34. Components of the effective elasticity material matrix as a function of the coating thickness. (Reprinted from *Comput. Math. Appl.*, 70, Stephan Heinze, Meysam Joulaian, Alexander Düster, Numerical homogenization of hybrid metal foams using the finite cell method, 1501–1517, © 2015, with permission from Elsevier.)

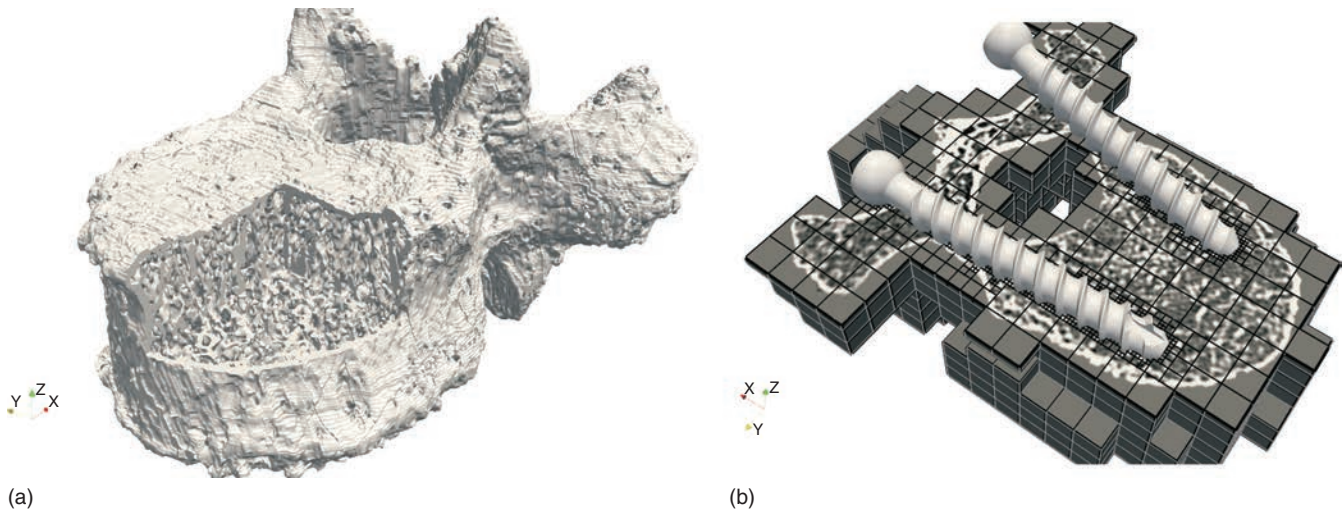


Figure 35. (a) HR-pQCT scan of a human vertebra. (b) Cut geometric model showing the finite cell grid with the local refinement and B-rep model of screws.

In contrast to these approaches, the FCM can employ, due to its high-order shape functions, cell sizes which are significantly larger than one voxel. In this example, unrefined cells with $27 \times 27 \times 20$ voxels are used. As the integration of cell matrices only relies on an inside-outside test, both geometric models can be used as they are: Each integration point tests if it is inside or outside a voxel of the HR-pQCT scan or of the B-rep model of the screw. If both tests are positive, a location inside the screw with the corresponding material properties is assumed. Furthermore, applying the hierarchical *hp-d* refinement sketched in Section 6.6, the critical zone in the vicinity of the interface of screw and bone can be resolved in detail; whereas in unstressed areas, a much coarser cell size can be applied. A cut through the combined vertebra-screw-model showing

the local refinement of cells toward the interface is displayed in Figure 35(b).

The finite cell analysis using the trunk space as Ansatz space yields for a polynomial degree $p = 4$ on the hierarchically refined mesh 1124 625 degrees of freedom. The computational time on a workstation with two 8-core Intel® Xeon® E5-2690 CPUs for an elastic analysis was less than 80 min. Figure 36(a) plots the displacement field for the described load case, whereas the other plots in Figure 36 show equivalent strains.

For a detailed study on validation and verification of the FCM for bone simulation demonstrating its high accuracy and reliability at low computational cost, refer Ruess *et al.* (2012).

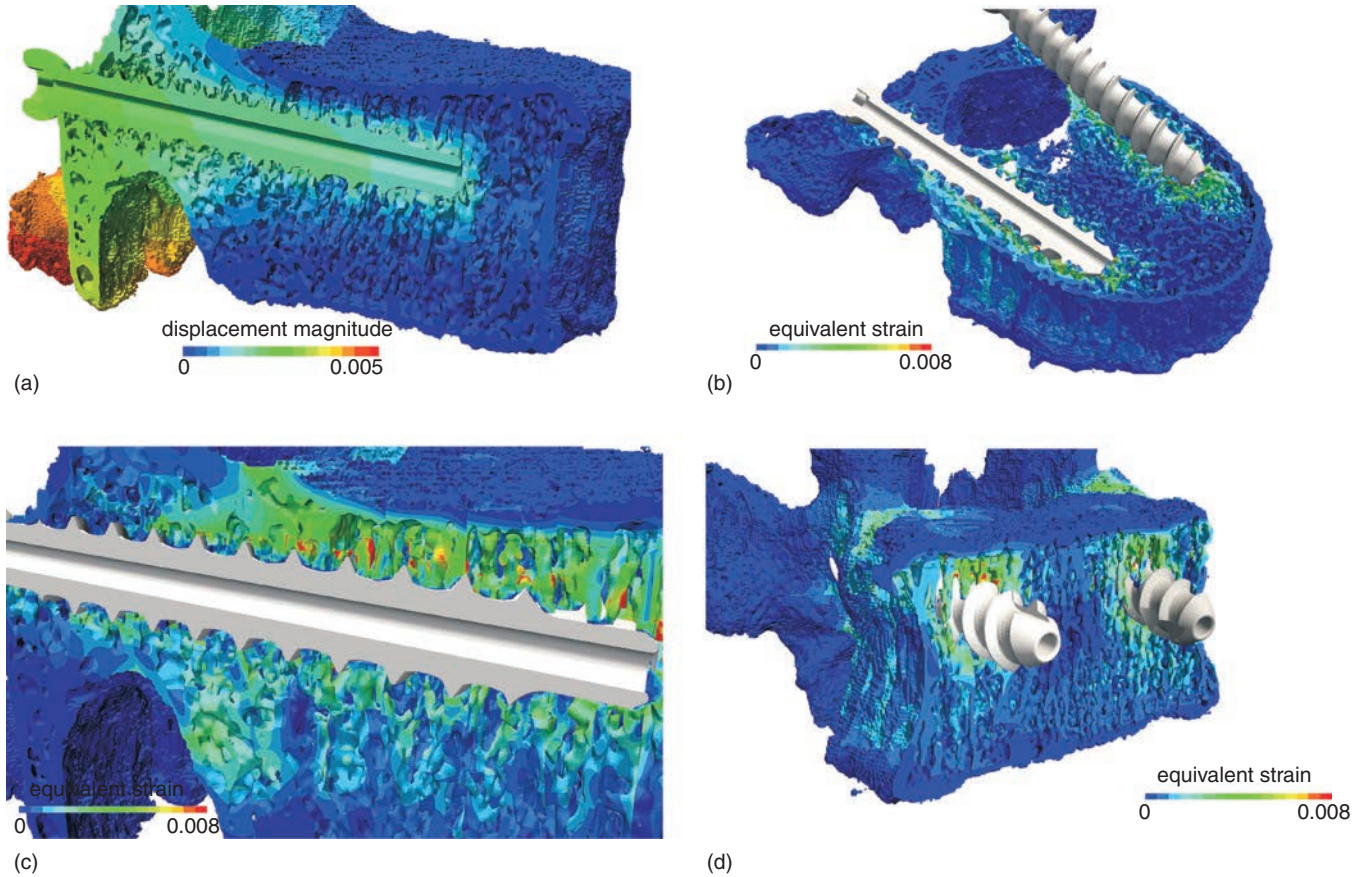


Figure 36. (a) Displacements. (b) Equivalent strains. (c,d) Local view of equivalent strains.

7 CONCLUSIONS

Two important features distinguish the p -version of the FEM from the conventional h -FEM: approximation spaces, constructed for (in principle) arbitrary polynomial order are used, and hierarchic *sequences* of approximate solutions are obtained by p -extension. This provides the basis for estimating and controlling numerical errors in terms of any quantity of interest. Since computed information is part of the engineering decision-making process, there is substantial demand for verified data. Other favorable properties of the p -FEM are its robustness with respect to locking effects and mesh distortion as well as high rates of convergence. Combining p -extension with properly designed meshes yields exponential rates of convergence for a large class of problems of practical interest.

While mesh generation for the p -FEM remains a challenging problem and, in particular in the case of 3D solid models more complex than for low-order elements, the combination with embedded domain techniques in the FCM

eliminates the meshing problem and offers large potential for close integration of geometric modeling and numerical analysis. Most features of a boundary-conforming p -FEM such as accuracy, robustness, and efficiency are equally valid for FCM. Furthermore, the variety of directly usable geometric models (B-rep models, CSG, and voxel-based models) opens the door for new fields of application in computational science and engineering. Although the FCM has been outlined here in the context of a p -FEM discretization, many of the findings concerning numerical integration of cut cells, trimmed geometries, and local refinement presented herein apply to IGA as well. Whether approximation spaces should be constructed in a p -FEM sense or, as in IGA, by spline functions depends on the specific field of application.

NOTES

1. In case $\Psi_i(u_{EX})$ is zero, absolute instead of a relative tolerance has to be checked.

2. StressCheck is a trademark of Engineering Software Research and Development, Inc., St. Louis, Missouri, USA (www.esrd.com).
3. The STL format is frequently applied in rapid prototyping and it is used to interact with stereolithography machines.

REFERENCES

- Abedian A, Parvizian J, Düster A, Khademyzadeh H and Rank E. Performance of different integration schemes in facing discontinuities in the finite cell method. *Int. J. Comput. Methods* 2013a; **10**:1350002/1–24.
- Abedian A, Parvizian J, Düster A and Rank E. The finite cell method for the J_2 flow theory of plasticity. *Finite Elem. Anal. Des.* 2013b; **69**:37–47.
- Abedian A, Parvizian J, Düster A and Rank E. Finite cell method compared to h -version finite element method for elasto-plastic problems. *Appl. Math. Mech.-Engl.* 2014; **35**:1239–1248.
- Actis R, Szabó BA and Schwab C. Hierarchic models for laminated plates and shells. *Comput. Methods Appl. Mech. Eng.* 1999; **172**:79–107.
- Ainsworth M and Oden JT. *A Posteriori Error Estimation in Finite Element Analysis*. John Wiley & Sons, Inc.: New York, 2000.
- Baaijens F. A fictitious domain/mortar element method for fluid-structure interaction. *Int. J. Numer. Methods Fluids* 2001; **35**:743–761.
- Babuška I and Elman HC. Some aspects of parallel implementation of the finite element method on message passing architectures. *J. Comput. Appl. Math.* 1989; **27**:157–189.
- Babuška I and Scapolla T. Computational aspects of the h -, p - and hp -versions of the finite element method. In *Advances in Computer Methods in Partial Differential Equations – VI*, Vichnevetsky R and Stepleman RS (eds). International Association for Mathematics and Computer Simulation (IMACS): New Brunswick, NY, 1987; 233–240.
- Babuška I and Strouboulis T. *The Finite Element Method and its Reliability*. Oxford University Press: Oxford, 2001.
- Babuška I and Suri M. The p - and hp -versions of the finite element method, an overview. *Comput. Methods Appl. Mech. Eng.* 1990; **80**:5–26.
- Babuška I and Suri M. On locking and robustness in the finite element method. *SIAM J. Numer. Anal.* 1992; **29**:1261–1293.
- Babuška I, Szabó BA and Katz IN. The p -version of the finite element method. *SIAM J. Numer. Anal.* 1981; **18**:515–545.
- Barthold FJ, Schmidt M and Stein E. Error estimation and mesh adaptivity for elastoplastic deformations. In *Proceedings of the 5th International Conference on Computational Plasticity, Complas V*, Barcelona, 1997.
- Barthold FJ, Schmidt M and Stein E. Error indicators and mesh refinements for finite-element-computations of elastoplastic deformations. *Comput. Mech.* 1998; **22**:225–238.
- Bindick S, Stiebler M and Krafczyk M. Fast kd-tree based hierarchical radiosity for radiative heat transport problems. *Int. J. Numer. Methods Eng.* 2011; **86**:1082–1100.
- Bishop J. Rapid stress analysis of geometrically complex domains using implicit meshing. *Comput. Mech.* 2003; **30**:460–478.
- Bröker H. *Integration von geometrischer Modellierung und Berechnung nach der p-Version der FEM*. PhD thesis, Lehrstuhl für Bauinformatik, Technische Universität München, 2001; published in Shaker Verlag: Aachen, ISBN: 3-8265-9653-6, 2002.
- Bungartz HJ, Griebel M and Zenger C. *Introduction to Computer Graphics*. Charles River Media, Inc.: Hingham, MA, 2004.
- Chen Q and Babuška I. Approximate optimal points for polynomial interpolation of real functions in an interval and in a triangle. *Comput. Methods Appl. Mech. Eng.* 1995; **128**:405–417.
- Chen Q and Babuška I. The optimal symmetrical points for polynomial interpolation of real functions in the tetrahedron. *Comput. Methods Appl. Mech. Eng.* 1996; **137**:89–94.
- Cheng KW and Fries TP. *Higher-order XFEM for curved strong and weak discontinuities*. *Int. J. Numer. Methods Eng.* 2009; **82**:564–590.
- Costabel M, Dauge M and Schwab C. Exponential convergence of hp -FEM for Maxwell equations with weighted regularization in polygonal domains. *Math. Models Methods Appl. Sci.* 2005; **15**(4):575–622.
- Cottrell JA, Hughes TJR and Bazilevs Y. *Isogeometric analysis: Towards Integration of CAD and FEM*. John Wiley & Sons, Ltd: Chichester, 2009.
- Dauge M, Düster A and Rank E. Theoretical and numerical investigation of the finite cell method. *J. Sci. Comput.* 2015; **26**:1–26.
- Del Pino S and Pironneau O. A fictitious domain based general PDE solver. In *Numerical Methods for Scientific Computing Variational Problems and Applications*, Kuznetsov Y, Neittanmaki P and Pironneau O (eds). CIMNE: Barcelona, 2003.
- Demkowicz L. *Computing with hp-Adaptive Finite Elements: One and Two Dimensional Elliptic and Maxwell Problems*, Chapman & Hall/CRC Applied Mathematics & Nonlinear Science. Chapman and Hall/CRC: Boca Raton, FL, 2006.
- Demkowicz L, Kurtz J, Pardo D, Paszyński M, Rachowicz W and Zdunek A. *Computing with hp-Adaptive Finite Elements: Three Dimensional Elliptic and Maxwell Problems with Applications*, Chapman & Hall / CRC Applied Mathematics & Nonlinear Science, Chapman and Hall/CRC: Boca Raton, FL, 2007.
- Duczek S and Gabbert U. Efficient integration method for fictitious domain approaches. *Comput. Mech.* 2015; **56**:725–738.
- Duczek S, Joulaian M, Düster A and Gabbert U. Numerical analysis of Lamb waves using the finite and spectral cell method. *Int. J. Numer. Methods Eng.* 2014; **99**:26–53.
- Düster A. *High Order Finite Elements for Three-Dimensional, Thin-Walled Nonlinear Continua*. PhD thesis, Lehrstuhl für Bauinformatik, Technische Universität München, 2001; published in Shaker Verlag: Aachen, ISBN: 3-8322-0189-0, 2002.
- Düster A and Rank E. The p -version of the finite element method compared to an adaptive h -version for the deformation theory of plasticity. *Comput. Methods Appl. Mech. Eng.* 2001; **190**:1925–1935.
- Düster A and Rank E. A p -version finite element approach for two- and three-dimensional problems of the J_2 flow theory with

- non-linear isotropic hardening. *Int. J. Numer. Methods Eng.* 2002; **53**:49–63.
- Düster A, Bröker H and Rank E. The p-version of the finite element method for three-dimensional curved thin walled structures. *Int. J. Numer. Methods Eng.* 2001; **52**:673–703.
- Düster A, Hartmann S and Rank E. p-FEM applied to finite isotropic hyperelastic bodies. *Comput. Methods Appl. Mech. Eng.* 2003; **192**:5147–5166.
- Düster A, Niggel A, Nübel V and Rank E. A numerical investigation of high-order finite elements for problems of elasto-plasticity. *J. Sci. Comput.* 2002; **17**:397–404.
- Düster A, Parvizian J, Yang Z and Rank E. The finite cell method for three-dimensional problems of solid mechanics. *Comput. Methods Appl. Mech. Eng.* 2008; **197**:3768–3782.
- Düster A, Scholz D and Rank E. *pq*-Adaptive solid finite elements for three-dimensional plates and shells. *Comput. Methods Appl. Mech. Eng.* 2007; **197**:243–254.
- Düster A, Sehlhorst HG and Rank E. Numerical homogenization of heterogeneous and cellular materials utilizing the finite cell method. *Comput. Mech.* 2012; **50**:413–431.
- Fries TP and Omerović S. Higher-order accurate integration of implicit geometries. *Int. J. Numer. Methods Eng.* 2015; **106**(5):323–371.
- Glowinski R and Kuznetsov Y. Distributed Lagrange multipliers based on fictitious domain method for second order elliptic problems. *Comput. Methods Appl. Mech. Eng.* 2007; **196**:1498–1506.
- Gordon WJ and Hall ChA. Construction of curvilinear co-ordinate systems and applications to mesh generation. *Int. J. Numer. Methods Eng.* 1973a; **7**:461–477.
- Gordon WJ and Hall ChA. Transfinite element methods: blending function interpolation over arbitrary curved element domains. *Numer. Math.* 1973b; **21**:109–129.
- Grisvard P. *Elliptic Problems in Nonsmooth Domains*. Pitman Advanced Publishing Program: Boston, MA, 1985.
- Guo B and Babuška I. The hp version of the finite element method. *Comput. Mech.* 1986; **1**:121–41.
- Heinze S, Joulaian M and Düster A. Numerical homogenization of hybrid metal foams using the finite cell method. *Comput. Math. Appl.* 2015a; **35**:1–35.
- Heinze S, Joulaian M, Düster A. Numerical homogenization of hybrid metal foams using the finite cell method. *Comput. Math. Appl.* 2015b; **701**(70):1501–1517.
- Heinze S, Joulaian M and Egger H and Düster A. Efficient computation of cellular materials using the finite cell method. *Proc. Appl. Math. Mech.* 2014; **14**:251–252.
- Heißerer U, Hartmann S, Düster A and Yosibash Z. On volumetric locking-free behavior of p-version finite elements under finite deformations. *Commun. Numer. Methods Eng.* 2008a; **24**:1019–1032.
- Heißerer U, Hartmann S, Düster A, Bier W, Yosibash Z and Rank E. p-FEM for finite deformation powder compaction. *Comput. Methods Appl. Mech. Eng.* 2008b; **197**:727–740.
- Hencky H. Zur Theorie plastischer Deformationen und der hierdurch im Material hervorgerufenen Nebenspannungen. In *Proceedings of the 1st International Congress on Applied Mechanics*, Delft, 1924.
- Holzer S and Yosibash Z. The p-version of the finite element method in incremental elasto-plastic analysis. *Int. J. Numer. Methods Eng.* 1996; **39**:1859–1878.
- Hubrich S, Joulaian M and Düster A. Numerical integration in the finite cell method based on moment-fitting. In *Proceedings of 3rd ECCOMAS Young Investigators Conference, 6th GACM Colloquium*, Aachen, Germany, 2015;1–4.
- Huiskes R and Chao EYS. A survey of finite element analysis in orthopedic biomechanics: the first decade. *J. Biomech.* 1983; **16**(6):385–409.
- Joulaian M and Düster A. Local enrichment of the finite cell method for problems with material interfaces. *Comput. Mech.* 2013; **52**:741–762.
- Joulaian M, Duzcek S, Gabbert U and Düster A. Finite and spectral cell method for wave propagation in heterogeneous materials. *Comput. Mech.* 2014; **54**:661–675.
- Joulaian M, Hubrich S and Düster A. Numerical integration of discontinuities on arbitrary domains based on moment fitting. *Comput. Mech.* 2016; doi: 10.1007/s00466-016-1273-3.
- Keyak JH and Falkinstein Y. Comparison of in situ and in vitro CT scan-based finite element model predictions of proximal femoral fracture load. *Med. Eng. Phys.* 2003; **25**(9):781–787.
- Királyfalvi G and Szabó BA. Quasi-regional mapping for the p-version of the finite element method. *Finite Elem. Anal. Des.* 1997; **27**:85–97.
- Kudela L, Zander N, Bog T, Kollmannsberger S and Rank E. Efficient and accurate numerical quadrature for immersed boundary methods. *Adv. Model. Simul. Eng. Sci.* 2015; **2**:1–22.
- Kudela L, Zander N, Kollmannsberger S and Rank E. Smart octrees: accurately integrating discontinuous functions in 3D. *Comput. Methods Appl. Mech. Eng.* 2016; **306**:406–426.
- Löhner R, Baum JD, Mestreau E, Sharov D, Charman C and Pelessone D. Adaptive embedded unstructured grid methods. *Int. J. Numer. Methods Eng.* 2004; **60**:641–660.
- Löhner R, Cebra JR, Camelli FF, Baum JD, Mestreau EL and Soto OA. Adaptive Embedded/Immersed unstructured grid techniques. *Arch. Comput. Meth. Eng.* 2007; **14**:279–301.
- Melenk JM and Babuška I. The partition of unity finite element method: basic theory and applications. *Comput. Methods Appl. Mech. Eng.* 1996; **39**:289–314.
- Melenk M and Wohlmuth B. On residual-based a-posteriori error estimation in hp-FEM. *Adv. Comput. Math.* 2001; **15**:311–331.
- Melenk M, Gerdes K and Schwab C. Fully discrete hp-finite elements: fast quadrature. *Comput. Methods Appl. Mech. Eng.* 2001; **190**:4339–4369.
- Mittal R and Iaccarino G. Immersed boundary method. *Annu. Rev. Fluid Mech.* 2005; **37**:239–260.
- Mousavi SE and Sukumar N. Numerical integration of polynomials and discontinuous functions on irregular convex polygons and polyhedrons. *Comput. Mech.* 2011; **47**:535–554.
- Müller B, Kummer F and Oberlack M. Highly accurate surface and volume integration on implicit domains by means of moment-fitting. *Int. J. Numer. Methods Eng.* 2013; **96**(8):512–528.
- Naghdi PM. *The Theory of Shells and Plates*. Springer-Verlag: Berlin Heidelberg, 1973.

- Neittaanmäki P and Tiba D. An embedding of domains approach in free boundary problems and optimal design. *SIAM J. Control Optim.* 1995; **33**:1587–1602.
- Netz T, Düster A and Hartmann S. High-order finite elements compared to low-order mixed element formulations. *Z. Angew. Math. Mech.* 2013; **93**:163–176.
- Noël AT and Szabó BA. Formulation of geometrically non-linear problems in the spatial reference frame. *Int. J. Numer. Methods Eng.* 1997; **40**:1263–1280.
- Nübel V, Düster A and Rank E. Adaptive vector integration as an efficient quadrature scheme for p-version finite element matrices. In *Proceedings of the European Conference on Computational Mechanics*, Cracow, 2001.
- Parvizian J, Düster A and Rank E. Finite cell method–h- and p-extension for embedded domain problems in solid mechanics. *Comput. Mech.* 2007; **41**:121–133.
- Parvizian J, Düster A and Rank E. Topology optimization using the finite cell method. *Optim. Eng.* 2012; **13**:57–78.
- Peskin C. The immersed boundary method. *Acta Numer.* 2002; **11**:1–39.
- Pitkäranta J. The problem of membrane locking in finite element analysis of cylindrical shells. *Numer. Math.* 1992; **61**:523–542.
- Ramière I, Angot P and Belliard M. A fictitious domain approach with spread interface for elliptic problems with general boundary conditions. *Comput. Methods Appl. Mech. Eng.* 2007; **196**:766–781.
- Ranjbar M, Mashayekhi M, Parvizian J, Düster A and Rank E. Using the finite cell method to predict crack initiation in ductile materials. *Comput. Mater. Sci.* 2014; **82**:427–434.
- Rank E. Adaptive remeshing and h-p domain decomposition. *Comput. Methods Appl. Mech. Eng.* 1992; **101**:299–313.
- Rank E and Babuška I. An expert system for the optimal mesh design in the hp-version of the finite element method. *Int. J. Numer. Methods Eng.* 1987; **24**:2087–2106.
- Rank E, Bröker H, Düster A, Krause R and Rucker M. The p-version of the finite element method for structural problems. In *Error-Controlled Adaptive Finite Elements in Solid Mechanics*, Stein E (ed.). John Wiley & Sons, Inc.: New York, 2002; 263–307.
- Rank E, Kollmannsberger S, Sorger Ch and Düster A. Shell finite cell method: a high order fictitious domain approach for thin-walled structures. *Comput. Methods Appl. Mech. Eng.* 2011; **200**:3200–3209.
- Rank E, Krause R and Preusch K. On the accuracy of p-version elements for the Reissner-Mindlin plate problem. *Int. J. Numer. Methods Eng.* 1998; **43**:51–67.
- Rank E, Rucker M, Düster A and Bröker H. The efficiency of the p-version finite element method in a distributed computing environment. *Int. J. Numer. Methods Eng.* 2001; **52**:589–604.
- Rank E, Ruess M, Kollmannsberger S, Schillinger D and Düster A. Geometric modeling, isogeometric analysis and the finite cell method. *Comput. Methods Appl. Mech. Eng.* 2012; **249–252**:104–115.
- Ruess M, Schillinger D, Bazilevs Y, Varduhn V and Rank E. Weakly enforced essential boundary conditions for NURBS-embedded and trimmed NURBS geometries on the basis of the finite cell method. *Int. J. Numer. Methods Eng.* 2013; **10**:811–846.
- Ruess M, Tal D, Trabelsi N, Yosibash Z and Rank E. The finite cell method for bone simulations: verification and validation. *Biomech. Model Mechanobiol.* 2012; **11**(3–4):425–437.
- Saul’ev VK. A method for automatization of the solution of boundary value problems on high performance computers. *Dokl. Akad. Nauk SSSR* 1962; **144**:497–500 (in Russian). English translation in *Sov. Math. Dokl.* 1962; **3**:763–766.
- Saul’ev VK. On solution of some boundary value problems on high performance computers by fictitious domain method. *Siberian Math. J.* 1963; **4**:912–925.
- Schillinger D and Rank E. An unfitted hp adaptive finite element method based on hierarchical B-splines for interface problems of complex geometry. *Comput. Methods Appl. Mech. Eng.* 2011; **200**:3358–3380.
- Schillinger D, Dedé L, Scott MA, Evans JA, Borden MJ, Rank E and Hughes TJR. An isogeometric design-through-analysis methodology based on adaptive hierarchical refinement of NURBS, immersed boundary methods, and T-spline CAD surfaces. *Comput. Methods Appl. Mech. Eng.* 2012a; **249–252**:116–150.
- Schillinger D, Düster A and Rank E. The hp-d-adaptive finite cell method for geometrically nonlinear problems of solid mechanics. *Int. J. Numer. Methods Eng.* 2012b; **89**:1171–1202.
- Schillinger D, Ruess M, Zander N, Bazilevs Y, Düster A and Rank E. Small and large deformation analysis with the p- and B-spline versions of the finite cell method. *Comput. Mech.* 2012c; **50**:445–478.
- Schwab Ch. A-posteriori modeling error estimation for hierarchic plate models. *Numer. Math.* 1996; **74**:221–259.
- Schwab Ch. *p- and hp-Finite Element Methods*. Oxford University Press: Oxford, 1998.
- Stein E. *Error-Controlled Adaptive Finite Elements in Solid Mechanics*. John Wiley & Sons: West Sussex, England, 2002.
- Stein E, Barthold FJ, Ohnimus S and Schmidt M. Adaptive finite elements in elastoplasticity with mechanical error indicators and Neumann-type estimators. In *Proceedings of the Workshop on New Advances in Adaptive Computational Mechanics*, Cachan, 1997.
- Sudhakar Y and Wall WA. Quadrature schemes for arbitrary convex/concave volumes and integration of weak form in enriched partition of unity methods. *Comput. Methods Appl. Mech. Eng.* 2013; **158**:39–54.
- Sudhakar Y, Moitinho de Almeida JP and Wall WA. An accurate, robust, and easy-to-implement method for integration over arbitrary polyhedra: application to embedded interface methods. *J. Comput. Phys.* 2014; **273**:393–415.
- Szabó BA. The p- and hp-versions of the finite element method in solid mechanics. *Comput. Methods Appl. Mech. Eng.* 1990; **80**:185–195.
- Szabó BA. Mesh design for the p-version of the finite element method. *Comput. Methods Appl. Mech. Eng.* 1986; **55**:181–197.
- Szabó BA and Babuška I. Computation of the amplitude of stress singular terms for cracks and reentrant corners. In *Fracture Mechanics: Nineteenth Symposium*, Cruse T (ed.), ASTM International: Philadelphia, PA, 1988; 101–124.
- Szabó BA and Babuška I. *Finite Element Analysis*. John Wiley & Sons, Inc.: New York, 1991.
- Szabó BA and Babuška I. *Introduction to Finite Element Analysis: Formulation, Verification and Validation*. John Wiley & Sons, Ltd: Chichester, 2011.
- Szabó BA and Mehta AK. p-Convergent finite element approximations in fracture mechanics. *Int. J. Numer. Methods Eng.* 1978; **12**:551–560.

- Szabó BA and Sahrman GJ. Hierarchic plate and shell models based on p -extension. *Int. J. Numer. Methods Eng.* 1988; **26**(8):1855–1881.
- Szabó BA, Actis R and Holzer S. Solution of elastic-plastic stress analysis problems by the p -version of the finite element method. In *Modeling, Mesh Generation, and Adaptive Numerical Methods for Partial Differential Equations, IMA Volumes in Mathematics and its Applications*, vol. 75, Babuška I and Flaherty J (eds). Springer: New York, 1995; 395–416.
- Ventura G. On the elimination of quadrature subcells for discontinuous functions in the extended finite-element method. *Int. J. Numer. Methods Eng.* 2006; **66**:761–795.
- Ventura G and Benvenuti E. Equivalent polynomials for quadrature in Heaviside function enriched elements. *Int. J. Numer. Methods Eng.* 2014; **102**:688–710.
- Vogelius M. An analysis of the p -version of the finite element method for nearly incompressible materials – uniformly valid optimal estimates. *Numer. Math.* 1983; **41**:39–53.
- Vos PEJ, Loon R and Sherwin SJ. A comparison of fictitious domain methods appropriate for spectral/hp element discretizations. *Comput. Methods Appl. Mech. Eng.* 2008; **197**:2275–2289.
- Wirth A, Müller R, Lenthe H. The discrete nature of trabecular bone microarchitecture affects implant stability. *J. Biomech.* 2012; **45**(6):1060–1067.
- Yang Z, Kollmannsberger S, Düster A, Ruess M, Garcia E, Burgkart R and Rank E. Non-standard bone simulation: interactive numerical analysis by computational steering. *Comput. Visual. Sci.* 2012a; **14**:207–216.
- Yang Z, Ruess M, Kollmannsberger S, Düster A and Rank E. An efficient integration technique for the voxel-based Finite Cell Method. *Int. J. Numer. Methods Eng.* 2012b; **91**:457–471.
- Yosibash Z and Szabó B. Convergence of stress maxima in finite element computations. *Commun. Numer. Methods Eng.* 1994; **10**:683–697.
- Zander N, Bog T, Elhaddad M, Espinoza R, Hu H, Joly A, Wu C, Zerbe P, Düster A, Kollmannsberger S, Parvizian J, Ruess M, Schillinger D and Rank E. FCMLab: a finite cell research toolbox for MATLAB. *Adv. Eng. Softw.* 2014; **74**:49–63.
- Zander N, Bog T, Kollmannsberger S, Schillinger D and Rank E. Multi-level hp-adaptivity: high-order mesh adaptivity without the difficulties of constraining hanging nodes. *Comput. Mech.* 2015; **55**:499–517.
- Zander N, Kollmannsberger S, Ruess M, Yosibash Z and Rank E. The finite cell method for linear thermoelasticity. *Comput. Math. Appl.* 2012; **64**:3527–3541.

FURTHER READING

- Babuška I, Whiteman JR and Strouboulis T. *Finite Elements: An Introduction to the Method and Error Estimation*. Oxford University Press: Oxford, 2010.
- Simo JC and Hughes TJR. *Computational Inelasticity*. Springer-Verlag: New York, 1998.
- Wriggers P. *Nonlinear Finite Element Methods*. Springer-Verlag: Berlin, Heidelberg, 2008.